SRFS Teleinfra

LOW-COST ANTENNA ARRAY BASED DRONE TRACKING DEVICE FOR OUTDOOR ENVIRONMENT

Plot no 10 Shiv Vihar A Block Najafgarh Nala Road
Vikasnagar Uttam Nagar New Delhi-110059

Contents

1. Introduction

Direction of arrival (DoA) approaches are now used in a wide range of applications, from classic wireless communication systems and rescue operations to GNSS systems and drone monitoring in public and private events. Unmanned Aerial Vehicles (UAVs) have been a major source of worry for airspace control agencies and the military in recent years because to potential terrorist strikes and criminal operations. In 2015, there were over 900 incidents between drones and planes in the United States , while in April 2016, an unmanned aerial vehicle (UAV) approached a plane landing at London's Heathrow airport .
In 2016, four drones infiltrated Dubai International Airport, one of the busiest in the world, disrupting landings and take-offs and triggering an outage. In October 2017 in Canada, the first reported collision of a drone and a commercial airplane has occurred and, still in 2017, an UAV invaded the Congonhas airport, Brazil, causing an estimated loss of approximately 1 million Reais due to the interruption of its services . Most recently, in December 2018 a total of 155 flights have been canceled and about 10 thousand passengers have been disrupted by drones flying over one of the UK's busiest airports, the Gatwick Airport .

In addition, and show cases of drones in football stadiums, threatening the fans safety. As shown before, these vehicles can, by carelessness, cause millions in losses. Therefore, recently police forces and security companies have drawn their attention to drone tracking devices in order to provide the safeness of citizens and clients. In this sense, the development of low-cost devices for drone tracking is fundamental to fit such demands. In order to detect the presence of drones and to track them, there is a variety of mechanical, optical or antenna array-based solutions in the market. For instance, the mechanical solution in detects a drone within 3 km for targets up to 55 cm in diameter, and classifies the model of the drone within 1.1 km.

The position accuracy (azimuth) in is 1. In, a rechargeable portable drone tracking device can detect and indicate the direction of a drone in a 360_ azimuth even with weak Line of Sight (LoS) component. The device in allows the communication with other devices by using an Application Programming Interface (API) framework. No technical information and patent about the principles behind the device in and its DoA accuracy are provided.

In an antenna array-based system is shown to detect with a 1 km range and with 1 accuracy or with a 7 km range and with 3 accuracies. In an application has been proposed for drone detection. According to the developers, the app has an average range of 106 meters. The system allows the detection of almost 95 % of all types of drones. However, the solution does not indicate the position or the direction of the drone.
In a square shaped 16 element antenna array is connected to switches so that a four channel SDR can select four antennas at each side of the square, allowing a 360 DoA estimation in outdoor environments. Each side of the square performs a azimuth estimation.

According to the authors, three Yagi antennas were used as sources at specific points, and maximum DoA error of 5 is achieved. No information is provided about the real distance between the sources and the receive array. In DoA estimation using an electronically steerable parasitic array radiator (ESPAR) with 12 parasitic elements and one active monopole is performed for wireless sensor network (WSN) applications. The authors calibrated the ESPAR array using an anechoic chamber. Since the main subject of is the calibration, no measurement outdoor or indoor campaigns are performed by the authors.

In a four element of quasi-Yagi antenna array system is applied for DoA estimation using the MUSIC algorithm, whereas the Minimum Description Length (MDL) criterion is used to estimate the amount of multipath components. Only two measurements are performed for two specific positions showing an error of 1

No information is provided about the experimental scenario. In several DoA estimation techniques are compared considering a horizontal uniform linear array (ULA) with 12 elements inside an anechoic chamber. The measurements were conducted varying the DoA from -20 to 20 in steps of 4
. The DoA estimation errors were smaller than 2
. The Min-Norm approach MUSIC [15] although it has a higher standard deviation. Finally, in [56], the authors developed system using five-port reflectometers, that allows to simultaneously measure the DoA and Time of Arrival (ToA) of coherent and incoherent signals, connected to seven quasi-Yagi antennas, with one reflectometer for each antenna.
The MUSIC algorithm is applied for the DoA estimation, providing an error of 2 for one source and 0,5 for two sources. The measurements were performed in a non-reflective environment.
In this dissertation, it is proposed a low-cost antenna array-based drone tracking device for outdoor environments. To the best of our knowledge, there is no state-of-the-art low-cost off-the-shelf antenna array-based device applied to drone tracking. The drone tracking is a challenging task due to the several possible modulation schemes for the data transmission, propagation phenomena, such as multipath components, and the possible long operational
distances. In the next chapter, the simplified state-of-the-art antenna array-based solutions for DoA estimation in the literature is detailed.

The device proposed is divided into hardware and software parts. The hardware part of the proposed device is based on off-the-shelf components such as an omni-directional antenna array, a 4 channel Software Defined Radio (SDR) platform, a FPGA motherboard, and a laptop.

The software part includes state-of-the-art algorithms for model order selection (MOS), pre-processing and DoA estimation, including others specific pre-processing and calibration steps in order to remove random errors and increase the DoA accuracy. The state of- the-art algorithm Exponential Fitting Test (EFT) [6] is used for MOS. For pre-processing schemes, Spatial smoothing (SPS) [9], Forward Backward Averaging (FBA) [10, 11] and Vanderdoes Invariance Transformation (VIT) [12] are used. And finally, the DoA estimation used the Delay and Sum [13], Minimum Variance Distortion-less Response (MVDR) or Capon's beamformer [14], Multiple Signal Classification (MUSIC) [15] and Estimation of Signal Parameters via Rotation Invariance Techniques (ESPRIT) [16] algorithms. This work also makes a comparative approach between several MOS algorithms in order to choose the winner, which is used in the proposed device. Additionally presents individual results of improvement brought by each preprocessing algorithm and its influence on the accuracy of the DoA estimation.

To build a product, it is necessary to prove the feasibility of it. The frequencies used for communications by the UAVs in the market are very important in order to select the frequency range or the array to be used. In Survey research, presented in Table 1.1 selected a variety of popular companies and manufactures of UAVs and its three most highlighted models for amateur or professional civilian use. Some companies have '-' as model name, that means the company have only one or two models. Note that the most used frequencies are 2.4 GHz followed by 5 GHz. Therefore, the experiments of this dissertation, and the previous one [57], are focused on 2.4 GHz and 5.8 GHz, respectively. An additional contribution of this work is to provide the complete configuration of the Pixhawk controller for beginners. This configuration is important for future researchers to be able to continue work using UAVs and can be found in Attachment A. Building the array of antennas with low-cost hardware is a challenging proposition, since it deals with difficulties such as mutual coupling, phase calibration and hardware problems. In the remainder of this work is described each of these problems and the proposed solutions.

This thesis is divided as follows: Chapter 2, the formulation problem and data model is presented. Next, in Chapter 3, is presented the review of State of the Art for Model Order Selections Schemes and Direction of Arrival methods that are used in the proposed device. Then, in Chapter 4, it is proposed a low-cost antenna array-based drone tracking device for outdoor environments, including a complete description of the hardware and software, and the steps involved for assembling, calibration, and signal processing. In Section 5, the proposed solution is validated by means of measurement campaigns in an outdoor scenario 3

Table 1.1: Table of frequencies (in MHz) used on popular UAVs

Company	**Model$_1$ (M1)**	**Model$_2$ (M2)**	**Model$_3$ (M3)**	**433**	**902-928**	**2400-2483.5**	**5150-5850**
3D Robotics	Solo [60]	X8+ [61]	IRIS [62]	M2 e M3	M2 and M3	M1	
AeroEnvironment	Quantix [63]	-	-		M1		
Autel Robotics	EVO [64]	X-Star Premium [65]	X-Star [65]		M2	M1 and M3	M2 and M3
Blade	C. 220 BNF Basic [66]	Theory XL [67]	Torrent 110 [68]				M1, M2 and M3
DJI	Mavic 2 Pro [69]	Phantom 4 Pro [70]	Matrice 200 [71]			M1, M2 and M3	M1, M2 and M3
EHang	GhostDrone [72]	Falcon [73]	-			M1 and M2	M2
Flyability	Elios [74]	-	-			M1	
GoPro	Karma [75, 76]	-	-			M1	
Hubsan	X4 Air Pro [77]	X4 Plus [78]	X4 Pro [79]			M1, M2 and M3	M1 and M3
Ideafly	Storm - 800 [80]	Grasshopper F210 [81]	Poseidon-480 [82]			M1,M2 and M3	M2 and M3
Parrot SA	Anafi [83]	Bebop 2 [84]	Disco [85]			M1, M2 and M3	M1, M2 and M3
Powervision	PowerEgg [86]	PowerEye [87]	-			M1 and M2	
Redcat racing	Carbon 210 [88]	-	-			M1	M1
SkyDrones	Zangão [89, 90]	Pelicano [91, 90]	Strix-AG [92, 90]			M1 and M2	M3
Syma	X5SW [93]	X8 pro [94]	Z1 [95]			M1, M2 and M3	
traxxas	Aton [96]	QR-1 [97]	Latrax Alias [98]			M1, M2 and M3	
Udi RC	Discovery 2 plus [99]	Peregrine [100]	Predator [101]			M1, M2 and M3	
Walkera	Furious 215 [102]	Voyager 4 [103]	VITUS [104]			M1, M2 and M3	M1, M2 and M3
WL toys	Q696-A [105]	V383 Stuntdrone [106]	Q696-D [107]			M2 and M3	M1
Yuneec	Typhoon 4K [108]	Tornado H920 [109]	H520 [110]			M1,M2 and M3	M1, M2 and M3

2. Problem formulation and data model

We assume d far filed sources transmitting narrow-band signals. These planar wavefront signals impinge over a receive antenna array with M omni-directional elements uniformly and linearly disposed.

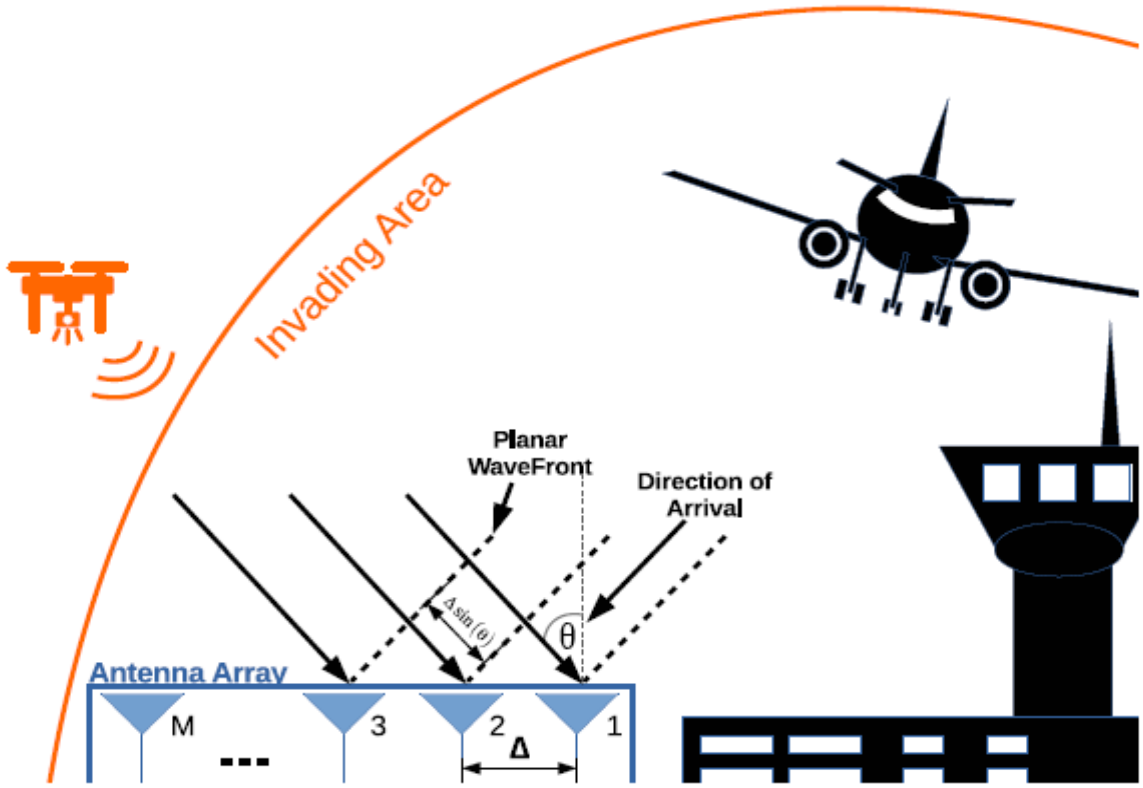

Figure 2.1: Formulation problem presenting the Uniform Linear Array with with M antennas and drawing impinging signals from an Unmanned Aerial Vehicle

The space _ between two adjacent antennas is equal to _ 2 , where _ is the wavelength of the carrier signal as presented in Fig. 2.1.

The received signals at the antenna array can be written in a matrix fashion as follows:

$$\mathbf{X} = \mathbf{AS} + \mathbf{N} \in \mathbb{C}^{M \times N}, \tag{2.1}$$

where $\mathbf{A} \in \mathbb{C}^{M \times d}$ is the steering matrix and its i-th steering vector is given by

$$\mathbf{a}(\mu_i) = \begin{bmatrix} 1 & e^{j\mu_i} & e^{2j\mu_i} & \dots & e^{j(M-1)\mu_i} \end{bmatrix}^{\mathrm{T}} \in \mathbb{C}^{M \times 1}, \tag{2.2}$$

where μ_i is the spatial frequency that can be mapped into the direction of arrival of the i-th source, θ_i, by the following expression: $\mu_i = \frac{2\pi\Delta \sin\theta_i}{\lambda}$. $\mathbf{S} \in \mathbb{C}^{d \times N}$ is the symbol matrix with N being the number of snapshots. $\mathbf{N} \in \mathbb{C}^{M \times N}$ stands for the noise matrix, whose elements are assumed as Complex-Valued Circularly Symmetric Gaussian and identically and independently distributed (i.i.d.).

Given (2.1) and assuming that the noise and the signal are uncorrelated, the covariance matrix can be computed by

$$\mathbf{R}_{\mathrm{XX}} = \mathrm{E}\{\mathbf{X}\mathbf{X}^{\mathrm{H}}\} = \mathbf{A}\mathbf{R}_{\mathrm{SS}}\mathbf{A}^{\mathrm{H}} + \mathbf{R}_{\mathrm{NN}}, \tag{2.3}$$

where $\mathbf{x}$ is one column vector from $\mathbf{X}$, $(\cdot)^{\mathrm{H}}$ is the Hermitian operator and $E\{\cdot\}$ is the expected value operator. In practice, the sample covariance matrix is calculated as follows:

$$\hat{\mathbf{R}}_{\mathrm{XX}} = \frac{\mathbf{X}\mathbf{X}^{\mathrm{H}}}{N} \in \mathbb{C}^{M \times M}. \tag{2.4}$$

The DoA techniques used along this paper exploit the sample covariance matrix in (2.4). As shown in Chapter 4, the matrix $\mathbf{X}$ is pre-processed before the computing of the covariance matrix $\hat{\mathrm{R}}_{\mathrm{XX}}$.

The goal of our proposed drone tracking device is to estimate the Direction of Arrival (DoA) θ_1 of the line of sight (LoS) signal component from a drone in an outdoor scenario. It is assumed that there is no obstruction of the LoS component. Therefore, the LoS component is assumed to have the greatest power in comparison with the Non-LoS components. Mathematically, it is expressed as

$$||\mathrm{a}(\mu_1)\mathrm{s}(\mu_1)||_{\mathrm{F}} > ||\mathrm{a}(\mu_i)\mathrm{s}(\mu_i)||_{\mathrm{F}}, \tag{2.5}$$

for $i = 2, \dots, d$. The operator $||\cdot||_{\mathrm{F}}$ stands for the Frobenius norm and d is the model order,

3.Literature Review

In this chapter are presented all the methods used to construct the proposed low cost antenna array based drones tracking device for outdoor environments. First of all, in Section 3.1 the Model Order Selection (MOS) schemes, which define the number of UAVs present in the scanned airspace and are a requirement for some DoA schemes, are described. Next, to provide improved accuracy in DoA schemes, preprocessing algorithms are presented in Section 3.2. Finally, in Section 3.3 the best-known DoA literature schemes are reviewed.

3.1 Model Order selection methods

One of the prerequisites for proper operation of the proposed device lies in a good selection of the matrix X obtained from the array. In other words, the noise only case needs to be avoided. One of the ways of this selection is by estimating the order of the model. Concluding, the device only calculates the Direct of Arrival (DoA) if it is in the presence of a signal. In addition, several DoA estimation algorithms depend on the knowledge of the model order. In the real world we do not know how many signals are arriving in our receiver array, so several techniques were proposed in the literature in order to estimate this number of sources. It can be classified as eigenvalues or subspace based and are usually called model order selection (MOS) techniques. In this chapter, the used methods are described, and the results of this techniques are drawn in Chapter 5.

3.1.1 Information Theoretic Criteria

Akaike's Information Criterion (AIC) [1], Minimum Description Length (MDL) [2] and Efficient Detection Criterion (EDC) [3] have similar expressions with different penalty functions. Therefore, they are classified as Information Theoretic Criteria (ITC). Due to the contribution in [111], that give a good performance with the expression for AIC and MDL, they are referred and used as benchmarks. A general expression is used in ITC methods and is given by

$$J(P) = -N(M-P)\log\left(\frac{g(P)}{a(P)}\right) + p(P,M), \tag{3.1}$$

where P is the candidate value to the estimated model order $\hat{d}$, which is obtained minimizing the $J(P)$. $g(P)$ and $a(P)$ are the geometric and arithmetic mean of P smallest eigenvalues λ_i of the ascending sorted main diagonal of a covariance matrix $\hat{\mathbf{R}}_{\mathbf{XX}}$ defined in (2.4). The $p(P,M)$ is a function of the number of independent parameters called penalty function and each method defines its own.

The MDL log-likelihood criterion is defined by

$$\mathrm{MDL(P)} = -\log\left\{\frac{\prod_{\mathrm{i=P+1}}^{\mathrm{M}} \lambda_{\mathrm{i}}^{\frac{1}{\mathrm{M-P}}}}{\frac{1}{\mathrm{M-P}}\sum_{\mathrm{i=P+1}}^{\mathrm{M}} \lambda_{\mathrm{i}}}\right\}^{\mathrm{(M-P)N}} + \frac{1}{2}\mathrm{p(M,N)logN}, \tag{3.2}$$

where M denotes number of sensors, N is the number of snapshots and λ_i is the i-th eigenvalue of the $\hat{\mathbf{R}}_{\mathbf{XX}}$. $p(\kappa)$ is the penalty function that change with the proprieties of the matrix and the preprocessing applied. It is defined as follows

$$p(M,N) = \begin{Bmatrix} P(2M-P+1)\text{For real matrices} \\ P(M+P+1)\text{For real FB - averaging} \\ P(2M-P)\text{For complex matrices} \\ 0.5P(2M-P+1)\text{For complex FB - averaging} \end{Bmatrix}. \tag{3.3}$$

For the AIC, the log-likelihood criterion is given by

$$\mathrm{AIC(P)} = -\log\left\{\frac{\prod_{\mathrm{i=P+1}}^{\mathrm{M}} \lambda_{\mathrm{i}}^{\frac{1}{\mathrm{M-P}}}}{\frac{1}{\mathrm{M-P}}\sum_{\mathrm{i=P+1}}^{\mathrm{M}} \lambda_{\mathrm{i}}}\right\}^{\mathrm{(M-P)N}} + \mathrm{p(M,N)}. \tag{3.4}$$

Finally, for the EDC, the log-likelihood criterion is given by

$$\mathrm{EDC(P)} = -\log\left\{\frac{\prod_{\mathrm{i=P+1}}^{\mathrm{M}} \lambda_{\mathrm{i}}^{\frac{1}{\mathrm{M-P}}}}{\frac{1}{\mathrm{M-P}}\sum_{\mathrm{i=P+1}}^{\mathrm{M}} \lambda_{\mathrm{i}}}\right\}^{\mathrm{(M-P)N}} + \mathrm{p(M,N)C_N}. \tag{3.5}$$

where C_N can be any function of N such that obey this two proprieties

Note that AIC, MDL, and EDC are divided in two parts. In the first part, the log-likelihood criterion function does not change, whilst the second part the penalty function (3.3) changes with the method. The result of the influence on eigenvalues made by increasing P causes the first part of the criterion to decrease but at the same time the second part to increase. Therefore, we vary P, in order to find the value that minimizes the AIC(P) and MDL(P). Then, the estimated number of sources is defined by ^ d = arg min P [MDL(P), AIC(P) or EDC(P)].

3.1.2 Stein's Unbiased Risk Estimator

In the more recent Stein's Unbiased Risk Estimator (SURE) approach [4], P if found in order to minimize the risk $\hat{R}(P)$ as follows

$$\begin{aligned} \hat{R}(P) &= (M-P)\hat{\sigma}_P^2 + 2\sigma^2 P + (\hat{\sigma}_P^4 - 2\hat{\sigma}_P^2\sigma^2\frac{4\hat{\sigma}_P^2\sigma^2}{N})\sum_{i=1}^{P}\frac{1}{\lambda_i} + C \\ C &= \frac{4\sigma^2}{N}\sum_{i=1}^{P}\sum_{j=P+1}^{M}\frac{\lambda_i - \hat{\sigma_P^2}}{\lambda_i - \lambda_j} + \frac{2\sigma^2}{N}P(P-1) - \frac{2\sigma^2}{N}(M-1)\sum_{i=1}^{P}\left(1 - \frac{\hat{\sigma}_P^2}{\lambda_i}\right), \end{aligned} \tag{3.7}$$

where $\hat{\sigma}_P^2 = \frac{1}{M-P}\sum_{i=P+1}^{M}\lambda_i$ and the noise variance σ^2 is estimated via Random Matrix Theory (RMT) algorithm defined in [4]. In the RMT, to estimate de noise variance, one of the steps uses a crude estimate of σ^2 with a certain percentile, about 25 and 30-th of smallest noise corrected eigenvalues, or even the median. Then, the estimated number of sources is defined by $\hat{d} = \arg\min_P \hat{R}(P)$.

3.1.3 RADOI

According to [5], in the eigenvalue based methods, the method called RADOI performs better for signals contaminated with colored noise. The main idea is that estimating $\hat{d}$ is equivalent to finding how many eigenvalues are associated to each signal and noise subspaces. The empirical functions g_1 and g_2 are the discriminant functions related to the noise and signal subspaces respectively, and are given by

$$g_1(P) = \frac{\lambda_{P+1}}{\sum_{i=2}^{M}\lambda_i}, \quad g_2(P) = \frac{\xi_P}{\sum_{i=1}^{M-1}\xi_i}, \quad P = 1, \cdots, M-1 \tag{3.8}$$

where $\xi_P = 1 - \frac{\alpha(\lambda_P - \mu_P)}{\mu_P}$, $\mu_P = \frac{1}{M-P}\sum_{i=P+1}^{M}\lambda_i$ and $\alpha = \left[\frac{\lambda_P - \mu_P}{\mu_P}\right]^{-1}$ e λ contains the autocorrelation matrix eigenvalues.

Then, the estimated number of sources $\hat{d}$ is defined as the first positive value from the following expression

$$\mathrm{RADOI(P)} = \mathrm{g_1(P)} - \mathrm{g_2(P)}. \tag{3.9}$$

3.1.4 Exponential Fitting Test

The EFT [6] is based on the approximation that the profile of the ordered noise eigenvalues have an exponential behavior. The profile a (M;N) can be expressed as

$$a(M,N) = \sqrt{\frac{1}{2}\left(\frac{15}{M^2+2} - \sqrt{\frac{225}{(M^2+2)^2} - \frac{180M}{N(M^2-1)(M^2+2)}}\right)}. \tag{3.10}$$

Given that $\hat{d} = M - P^*$, the goal is to vary P such that we find P^* that $\hat{\lambda}_{M-P} \ll \lambda_{M-P}$, where $\hat{\lambda}_{M-P}$ and λ_{M-P} stands for predicted $(M-P)^{\text{th}}$ noise eigenvalue and $M-P$ actual eigenvalue, respectively. Note that the EFT assumes the smallest eigenvalue as a noise eigenvalue. Therefore, P varies from 1 to $M-1$. Using (3.10), the authors in [6] derived the following expression

$$\hat{\lambda}_{M-P} = (P+1)\cdot\left(\frac{1-a(P+1,N)}{1-a(P+1,N)^{P+1}}\right)\cdot\hat{\sigma}^2, \tag{3.11}$$

$$\hat{\sigma}^2 = \frac{1}{P+1}\sum_{i=0}^{N}\lambda_{M-i}, \tag{3.12}$$

where $\hat{\sigma}^2$ is the estimated noise power.

In order to improve further the performance of the EFT approach, thresholds coefficients η_P are computed using noise-only simulated data following Complex-Valued Circularly Symmetric Gaussian and identically and independently distributed (i.i.d.) as indicated in Chapter 2. Depending on the η_P, there are two hypothesis.

$$\mathrm{H}_P : \left|\frac{\lambda_{M-P} - \hat{\lambda}_{M-P}}{\hat{\lambda}_{M-P}}\right| \leq \eta_P \tag{3.13}$$

$$\bar{\mathrm{H}}_P : \left|\frac{\lambda_{M-P} - \hat{\lambda}_{M-P}}{\hat{\lambda}_{M-P}}\right| > \eta_P \tag{3.14}$$

where $\mathrm{H}_P : \lambda_{M-P}$ is a noise eigenvalue and $\bar{\mathrm{H}}_P : \lambda_{M-P}$ is a signal eigenvalue. In order to have all η_P depending on the $\mathrm{P_{fa}}$, it is possible define the $\mathrm{P_{fa}}$ as

$$\mathrm{P_{fa}} = \mathrm{Pr}[\hat{\mathrm{d}} \neq 0 | \mathrm{d} = 0] \tag{3.15}$$

where PR[.] is the probability operator. Note that the thresholds are obtained by Monte Carlo simulations carried out in the only-noise scenario following the steps in [6] and by choosing the following amount of realizations

$$\mathrm{I} = \frac{10}{\mathrm{P_{fa}}}. \tag{3.16}$$

Depending on the noise behaviour and the parameters of the scenario [112, 23], the $\mathrm{P_{fa}}$ can be extremely low. Therefore, the computational complexity of (3.16) can be prohibitive. In order to overcome such limitation, it is proposed in Appendix A an extrapolation approach to compute the thresholds for extremely low values of $\mathrm{P_{fa}}$.

3.1.5 SAMOS and ESTER

Different from the eigenvalue based, this Subsection presents the subspace based methods. Subspace based Automatic Model Order Selection (SAMOS) [8] and ESTimation ERror (ESTER) [7] use the shift invariance propriety and the steering matrix $\mathbf{A}$ having the Vandermonde structure.

ESTER is based on the DoA Estimating algorithm ESPRIT [16], which needs a prior value of model order d. According to [7], varying the candidate of model order $P \in \{1, \cdots, \min(\mathrm{M}, \mathrm{N})\}$ on algorithm, an erroneous P disturbs the estimation of sinusoids. In other words, for $P \neq d$ the shift invariance propriety is not valid. Based on this fact, the authors derive error bounds $\mathbf{E_E}(P)$ as follows

$$\begin{aligned} \mathbf{E}_{\mathrm{E}}(P) &= \mathbf{W}(P)_{\uparrow} - \mathbf{W}(P)_{\downarrow}\mathbf{\Phi}(P), \\ \mathbf{\Phi}(P) &= (\mathbf{W}(P)_{\downarrow})^{\dagger}(\mathbf{W}(P)_{\uparrow}), \end{aligned} \tag{3.17}$$

where $\mathbf{W}(P)_{\uparrow}$ contains the first left P eigenvectors as columns, $\mathbf{W}(P)_{\downarrow}$ contains the last right P eigenvectors as columns and $\{\cdot\}^{\dagger}$ denotes the pseudo-inverse operator.

Then the estimated number of sources $\hat{d}$ from ESTER [7], is defined as the value of P that maximizes the expression $\frac{1}{(||\mathbf{E_E}(P)||_2)^2}$, where $||\cdot||_2$ stands for the Euclidean vector norm (or 2-norm).

SAMOS [8] defines a matrix joining the $\mathbf{W}(P)_{\uparrow}$ and $\mathbf{W}(P)_{\downarrow}$ matrices, given expression $\mathbf{U}(P) = [\mathbf{W}(P)_{\uparrow}|\mathbf{W}(P)_{\downarrow}] \in (M-1) \times 2P$. According to the Authors, there are tree hypothesis to be analyzed:

- P > d, the rank of $\mathbf{U}(P)$ is increased by 2;
- P < d, the rank of $\mathbf{U}(P)$ is equal to min(2P,d);
- P = d, the $\lambda_{d+1}, \cdots, \lambda_{2d}$ singular values of $\mathbf{U}(P)$ are equal to zero.

Based on previous hypothesis the estimated number of order $\hat{d}$ is the value of P that

maximizes the expression $\frac{1}{E_S(P)}$, where $E_S(P)$ is defined as follows

$$E_S(P) = \frac{1}{P} \sum_{i=P+1}^{2P} \lambda_i^{tb}. \tag{3.18}$$

3.2 Pre-processing of data methods

In general, the preprocessing methods are used on the matrix X transforming it into a matrix Z that will be used by the other desired algorithms. Thus, with several concepts reviewed in this chapter, the preprocessing algorithms allow a better accuracy in the results of the DoA methods.

3.2.1 Spatial Smoothing

Spatial smoothing (SPS), proposed in [9] and discussed further in [25], has been used in coherent signals. The spatial smoothing technique introduced by [9] makes it possible to use DoAs algorithms in presence of arbitrary signal correlation under certain conditions. The most restrictive aspect os the SPS technique is that it requires an uniformed spaced array.

As our linear antenna array is a 4-element ULA, as well as respecting the above condition, it can be divided into two sub-arrays with $M_{\text{sub}} = 3$ elements each, $\{1, \cdots, M_{\text{sub}}\}$ forming the first sub-array and $\{2, \cdots, M_{\text{sub}} + 1\}$. It is called M_{sub} the number of sub-array sensors and M the array number of sensors. Is is applied SPS in X to get a measurement matrix $\mathbf{X_{SS}}$ that has a rank greater than or equal to d. A selection matrix J which selects the elements to be concatenated, is defined. This approach and $\mathbf{X_{SS}}$ is drawn as follows,

$$\mathbf{J}_l^{(M)} = \left[\mathbf{0}_{M_{\text{sub}} \times (l-1)} \mathbf{I}_{M_{\text{sub}}} \mathbf{0}_{M_{\text{sub}} \times (L-l)}\right], \quad l \in 1 \leq l \leq L, \tag{3.19}$$

$$\mathbf{X}_{SS} = \left[\mathbf{J}_1^{(M)}\mathbf{X} \quad \mathbf{J}_2^{(M)}\mathbf{X} \quad \dots \quad \mathbf{J}_L^{(M)}\mathbf{X}\right] \in \mathbb{C}^{M_{\text{sub}} \times LN}, \tag{3.20}$$

where L denotes the number of sub-arrays. Note that the number of sensors is reduced from M to M_{sub} after the spatial smoothing.

3.2.2 Forward Backward Averaging

One of the most commonly used preprocessing schemes, the Forward Backward Averaging (FBA) [10, 11] is used in a wide range of DoA methods. It effectively doubles the data consequently, improving the variances of the estimators. As other methods, FBA has requirements to be valid, such as samples be taken in a geometry that is also reversible, arrays must be centre-symmetric and the properties of the process under consideration be approximately

the same independent of the orientation of the time or space axis [10]. With this characteristics, FBA presents the desirable effect of reducing correlation between signals, as occurs in a multipath environment.

The basic operation of FBA relies on the fact that the matrix A remains the same even if its elements are reversed and complex conjugated [113]. It is possible to apply the FBA with this simple equations,

$$\mathbf{X}_{FB} = \frac{1}{\sqrt{2}}[\mathbf{X}, \mathbf{J}_1\mathbf{X}^*\mathbf{J}_2], \tag{3.21}$$

where $\mathbf{J}_1 \in \mathbb{C}^{M\times M}$ and $\mathbf{J}_2 \in \mathbb{C}^{N\times N}$ are selection matrices with 1's on the antidiagonal and 0's elsewhere.

3.2.3 Vandermonde Invariance Transformation

Different from interpolation methods [114, 115], the Vandermonde Invariance Transformation (VIT) [12] does not solve the physical array imperfections, it keeps the Vandermonde structure in a desired direction changing the others, making the uniform Vandermonde response of the array into one with a non uniform phase response. It also acts as beamformer conserving power at a direction of interest and reduces the power from the others.

VIT defines a $\mathbf{T}_{\text{vit}}(\text{r}) \in \mathbb{C}^{M\times M}$ and multiplies it by $\text{v}(\theta) = [1, e^{j\mu_i}, e^{2j\mu_i}, \cdots, e^{j(M-1)\mu_i}]^{\text{T}}$ containing a Vandermonde structure. It gives us the following result

$$\check{\text{v}}(\theta) = \mathbf{T}_{\text{vit}}(\text{r})\text{v}(\theta) = \left(\frac{e^{j\mu(\theta)} - r}{1 - r}\right)^{M-1} \cdot \begin{pmatrix} 1 \\ e^{j\nu(\theta)} \\ \vdots \\ e^{(M-1)\nu(\theta)} \end{pmatrix} \tag{3.22}$$

where $r \in \mathbb{C}$ are the complex roots of the polynomials, and can be chosen considering the noise suppression and the linearity of the output. Note that the original phase μ is mapped into a new phase ν, that can be expressed as follows

$$\nu = \arctan\left(\frac{2\text{K}.\sin(\theta)}{1 - \text{K}^2 + (1 + \text{K}^2).\cos(\theta)}\right), \tag{3.23}$$

where $K = \frac{r+1}{r-1}$ is a phase amplification.

To apply VIT on the received signal, it is built a transformation matrix $\mathbf{T}_{\text{f}}(K, \theta)$ in order to transform the received matrix $\mathbf{X}$ into a new matrix $\mathbf{Y}$ that has the proprieties described before. This transformation is drawn as follows

$$\mathbf{Y} = \mathbf{T}_{\text{f}}(r, \theta)\mathbf{X} \in \mathbb{C}^{M\times N}. \tag{3.24}$$

To find $\mathbf{T}_{\mathrm{f}}$, the matrix $\mathbf{T}_{\mathrm{vit}}$ is multiplied by a diagonal focusing matrix $\mathbf{F}(\theta) = \mathrm{diag}\{\mathrm{v}(\theta)\}$, where $\mathrm{v}(\theta) = [1, e^{j\mu_i}, e^{2j\mu_i}, \cdots, e^{j(M-1)\mu_i}]$ containing a Vandermonde structure and $\mathrm{diag}\{\cdot\}$ transforms its argument vector into the main diagonal of a diagonal matrix. Then, the $\mathbf{T}_{\mathrm{f}}$ is given by

$$\mathbf{T}_{\mathrm{f}}(K, \theta) = \mathbf{T}_{\mathrm{vit}}(\mathrm{r})\mathbf{F}(\theta). \tag{3.25}$$

Finally, the new data matrix $\mathbf{Y}$ is now used by the DoA algorithms obtaining a more precise DoA estimation with a cost of additional computational load.

3.3 Direction of Arrival methods

The Direction of Arrival of a signal has application in various areas such as radars and telecommunications. This is further boosted by the recent rise of Unmanned Aerial Vehicles (UAVs), thereby increasing the concern of airspace control bodies and even governments for illegal actions and even terrorist attacks. In this way the estimation of a target's location can be obtained using the Arrival Direction and some action could be taken. There are a variety of algorithms and their derivations, however in this work it is focused on the best-known classical methods of DoA detection, presented in this Section.

3.3.1 Beamformings and subspace based methods

The conventional beamforming methods have the basic idea of "scanning" the array in a specif direction and measure the output power. When the "scanned" direction is the same as a DoA of any signal, the output power will reach the maximum. The following equation address this concept

$$P(\theta) = \mathbf{w}^{\mathrm{H}}\mathbf{R}_{\mathrm{XX}}\mathbf{w} \tag{3.26}$$

where $\{\cdot\}^{\mathrm{H}}$ is the Hermitian operator and $\mathbf{R}_{\mathrm{XX}}$ is the covariance matrix. Most recent beamforming methods have been developed by measuring the output power (3.26) with different forms of the $\mathbf{w}$ called spatial filter as it is discussed in this Section.

3.3.1 Beamformings and subspace based methods

The conventional beamforming methods have the basic idea of "scanning" the array in a specif direction and measure the output power. When the "scanned" direction is the same as a DoA of any signal, the output power will reach the maximum. The following equation address this concept

$$P(\theta) = \mathbf{w}^{\mathrm{H}}\mathbf{R}_{\mathrm{XX}}\mathbf{w} \tag{3.26}$$

where $\{\cdot\}^{\mathrm{H}}$ is the Hermitian operator and $\mathbf{R}_{\mathrm{XX}}$ is the covariance matrix. Most recent beamforming methods have been developed by measuring the output power (3.26) with different forms of the $\mathbf{w}$ called spatial filter as it is discussed in this Section.

3.3.1.1 Delay and Sum

For the most simple algorithm Delay and Sum [13] when the scanned direction θ matches with the real DoA from the source the output power $P(\theta)$ will reach a peak or maximum point.

$$\mathbf{w}_{DS} = \frac{\mathbf{a}(\theta)}{\sqrt{\mathbf{a}^{\mathrm{H}}(\theta)\,\mathbf{a}(\theta)}}. \tag{3.27}$$

where $\mathbf{a}(\theta)$ is the steering vector in direction of θ with Vandermonde structure.

By inserting the weight vector (3.27) into (3.26), the output power as a function of angle of arrival is obtained as follows

$$P_{\mathrm{DS}}(\theta) = \frac{\mathbf{a}(\theta)^{H}\,\mathbf{R}_{\mathrm{XX}}\,\mathbf{a}(\theta)}{\mathbf{a}(\theta)^{H}\,\mathbf{a}(\theta)}. \tag{3.28}$$

This method has a poor resolution. However, to increase its accuracy, it is possible to add more sensors increasing the amount of storage data. In our case this is not possible since there is hardware limitations.

3.3.1.2 Capon

The Minimum Variance Distortion-less Response (MVDR) or Capon's beamformer [14] achieve the maximum power when the beam with θ matches the direction of a signal. The weight vector described from Capon is given by,

$$\mathbf{w}_{\mathrm{CAP}} = \frac{\mathbf{R}_{\mathrm{XX}}^{-1}\mathbf{a}(\theta)}{\mathbf{a}(\theta)^{\mathrm{H}}\mathbf{R}_{\mathrm{XX}}^{-1}\mathbf{a}(\theta)}. \tag{3.29}$$

Substituting (3.29) into (refeq:principalBeam), the spatial Capon power is given by

$$P_{\mathrm{CAP}}(\theta) = \frac{1}{\mathbf{a}(\theta)^{\mathrm{H}}\mathbf{R}_{\mathrm{XX}}^{-1}\mathbf{a}(\theta)}. \tag{3.30}$$

According to [113] CAPON works well when there is only one incoming signal present. However when there is more than one, the array output power contains signal contributions from the desired and undesired angles. In the particular desired direction, Capon minimizes the variance of the array output and allows the signal to pass from this direction with no distortion.

3.3.1.3 Multiple Signal Classification

The last beamformer present in this work is the MUltiple SIgnal Classification (MUSIC) [15]. It is based on noise subspace, which requires a prior knowledge of number of sources. The number of sources is used to select the first ordered largest d eigenvalues. Then, the noise subspace $\mathbf{V}_n$ is defined as a matrix formed by the eigenvectors related to the small ordered eigenvalues $\lambda_i \in \{d+1, \cdots, M\}$.

$$P_{\text{MUS}}(\theta) = \frac{1}{\mathbf{a}^{\text{H}}(\theta)\mathbf{V}_n\mathbf{V}_n^{\text{H}}\mathbf{a}(\theta)}, \tag{3.31}$$

As in the previous beamformers, the signals impinging on the array have DoAs given by the d tallest peaks from the spectrum $P_{\text{MUS}}(\theta)$.

Finally, Estimation of Signal Parameters via Rotation Invariance Techniques (ESPRIT) [16] is based on two identical subarrays in order to apply the shift invariance staggered in time. This method is similar to MUSIC at the point that is a subspace based approach, except to the fact that MUSIC uses the noise subspace and ESPRIT uses the signal subspace.

First, the Singular Value Decomposition (SVD) is applied to the data array $\mathbf{X}$. The SVD gives us the matrix $\mathbf{U} \in \mathbb{C}^{M\times M}$ of the right singular vectors, that are the eigenvectors from covariance matrix. Now the signal subspace $\mathbf{U}_s$ can be found by taking the first d eigenvectors, sorted according to eigenvalues, from $\mathbf{U}$. In other words, the matrix $\mathbf{U}$ can be rewritten as $\mathbf{U} = [\mathbf{U}_s|\mathbf{U}_n]$ with $\mathbf{U}_s \in \mathbb{C}^{M\times d}$.

As the steering matrix $\mathbf{A}$ generate the same subspace of $\mathbf{U}_s$, there is a nonsingular matrix $\mathbf{T} \in \mathbb{C}^{d\times d}$ such that $\mathbf{A} \approx \mathbf{U}_s\mathbf{T}$. The shift invariance propriety give us the assumption

$$\mathbf{J}_1\mathbf{U}_s\mathbf{T}\boldsymbol{\Phi} = \mathbf{J}_2\mathbf{U}_s\mathbf{T} \Leftrightarrow \mathbf{J}_1\mathbf{U}_s\boldsymbol{\Psi} = \mathbf{J}_2\mathbf{U}_s \tag{3.32}$$

where $\boldsymbol{\Psi} = \mathbf{T}\boldsymbol{\Phi}\mathbf{T}^{\dagger} \in \mathbb{C}^{d\times d}$ is a non singular matrix signal subspace rotating operator, $\{\cdot\}^{\dagger}$ being the pseudo-inverse operator, $\mathbf{J}_1$ and $\mathbf{J}_2$ are the selection matrices and $\boldsymbol{\Phi} = \text{diag}[\phi_1, ..., \phi_d]$ is the diagonal matrix that has the eigenvalues representing the estimates of phase factors $e^{j\mu}$ containing the DoA information.

As a result, if the signal subspace $\mathbf{U}_s$ can be estimated, $\boldsymbol{\Psi}$ and its eigenvalues containing DoAs information can then be found as follows

$$\boldsymbol{\Psi} = \mathbf{J}_1\mathbf{U}_s^{+}\mathbf{J}_2\mathbf{U}_s. \tag{3.33}$$

With $\boldsymbol{\Psi}$ and $\boldsymbol{\Phi}$ sharing the same eigenvalues, it is possible to apply the eigenvalue decomposition (EVD) on $\boldsymbol{\Psi}$ and obtain the ϕ_i where $1 \leq i \leq M$. Finally the DoA is found computing all the spatial frequencies μ that, if done the array remapping, can be mapped to θ.

$$\mu_i = \angle(\phi_i), i = 1, ..., d \tag{3.34}$$

$$\theta_i = \arcsin\left(-\frac{\lambda_i}{2\pi\Delta}\mu_i\right), i = 1, ..., d \tag{3.35}$$

4.Low-cost antenna array-based drone tracking device and Framework

In this Chapter was detailed the proposed low-cost antenna array-based drone tracking device. In Section 4.1, the steps for the hardware calibration are described. The calibration ensure all the four channels of the SDR are in phase, allowing the DoA estimation. In Section 4.2, it was presented the assembling of the components of the hardware of the proposed drone tracking device. In Section 4.3, a signal processing framework performed for DoA estimation was proposed.

The hardware components needed to build the low-cost drone tracking device are described in Table 4.1 and illustrated in the Fig. 4.1.

Table 4.1: List of hardware components used to build the low-cost drone tracking device

Item	Description
Software Defined Radios	4x4 MIMO platform ADFMCOMMS5 [30] (Fig. 4.1(b)), with two AD9361 [116] Integrated Circuits (ICs) that contains 2 transmitters and two receivers each, cover 70 MHz to 6.0 GHz and have a channel bandwidth of 200 kHz to 56 MHz.
FPGA motherboard	Zynq Zc702 [31] with FPGA Mezzanine Connectors (FMC) allowing scaling and customization with daughter cards (Fig. 4.1(a)).
4 antennas	Omni-directional, Dual Band 2400–2483.5, 4900–5875 MHz, +3.7 dBi of peak gain and linear polarization. [18] (Fig. 4.1(d) and 4.2).
4 Cables	Cable Assembly SMA 305 mm long [33] (Fig. 4.1(c)).
Power division component	RF Power Splitter, Combiner, Divider with SMA Female 4-Way inputs that covers 2.4 - 6.0 GHz
Personal portable computer	The computer is used to receive all the data from FPGA in order to be processed in the Matlab Software [117]

(a) uProc and FPGA motherboard [31]

(b) SDR 4x4 MIMO daughterboard [30]

(c) Cable SMA 305mm [33]

(d) Dual Band 2.4 & 5GHz [18]

(e) 4-Way Splitter 2.4-6GHz [32]

Figure 4.1: Hardware components for building the low cost drone tracking device

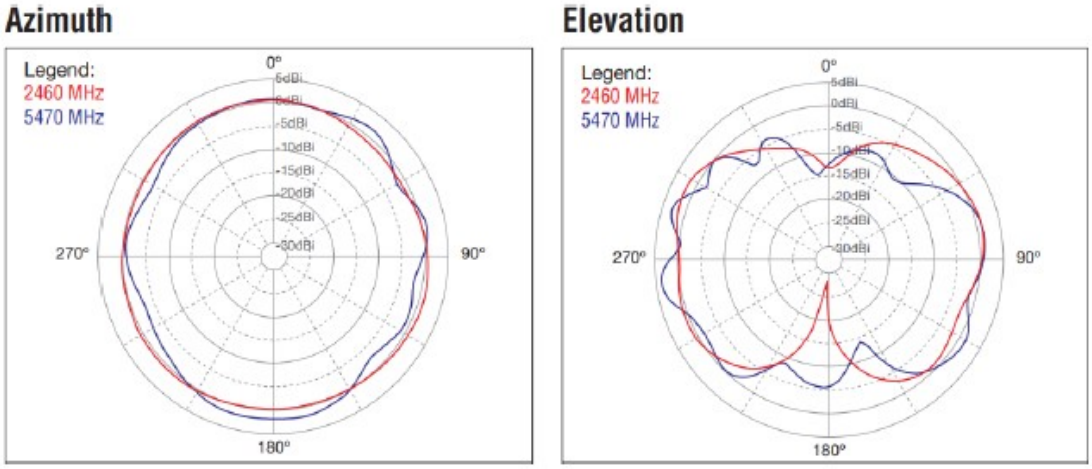

Figure 4.2: Radiation pattern for the antenna from Fig. 4.1(d). Image taken from [118]

4.1 Hardware assembling for the calibration

One of the big problems on practical antenna arrays is phase imbalance between the inputs of the SDR. This problem may be caused by hardware imperfection such as different lengths of the cables and tracks, multipath, different time of start on the oscillators or even by simple imperfections on manufacturing. The hardware vendor provides a software [17]

for clock synchronization of the local oscillator. However, this software does not perform phase calibration. This problem can be solved by a filter that multiplies the signal received by an exponential of the negatived phase error. This phase error is obtained measuring the difference of phase between the inputs of an arrived signal that is sent from a TX output, coming through a power divider with four output signals with the same power and four cables of equal length. The mathematical approach will be explained in Subsection 4.3.1. In order to perform the phase calibration, first the hardware components are assembled according to Fig. 4.3. Note that the SDR transmits a signal from one channel and receives it in four channels that should be calibrated, such that all receive channels are in phase.

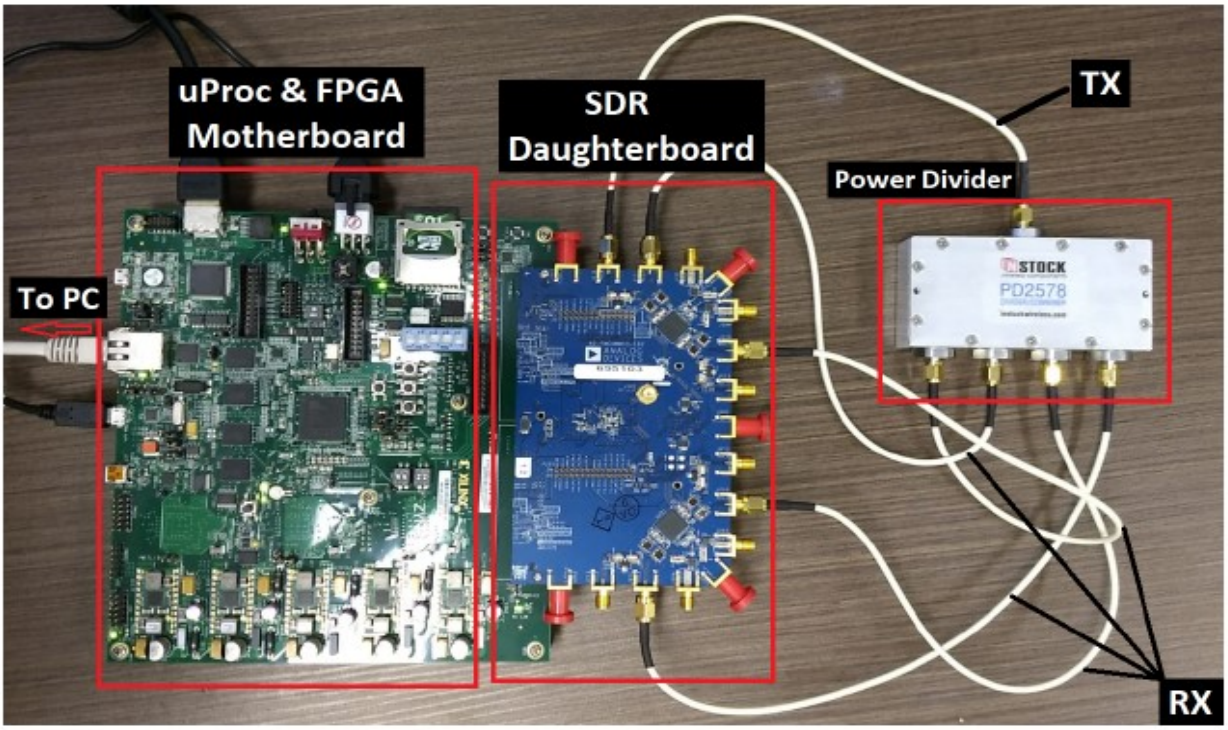

Figure 4.3: Assembled components for the hardware calibration of four receive channels. The components are a microprocessor (uProc) and FPGA motherboard, a SDR, a power divider and cables.

As shown in Fig. 4.3, the SDR [30] with two AD9361 [116] is connected to a microprocessor and FPGA motherboard [31], that configures the SDR and transmit the SDR data to PC through the UTP cable. Note that the cables [33] for calibration should have the same length. Moreover, a power divider component [32] is included in order to lead the signal to the four receive channels at the same time, and to reduce the power of the transmitted signal to avoid damaging.

4.2 Hardware assembling for the drone tracking measurement campaign

After the hardware has been calibrated, the next step is to assemble it in order to perform the measurements. The four elements omni-directional antenna array is connected to the calibrated hardware composed by the FPGA motherboard and SDR daughterboard according to Fig. 4.4. Each antenna is dual band (from 2400 MHz to 2483.5 MHz and from 4900 MHz to 5875 MHz) [18] and has linear polarization with 3.7 dBi of gain. The space between two consecutive antennas is equal to 59:9 mm.

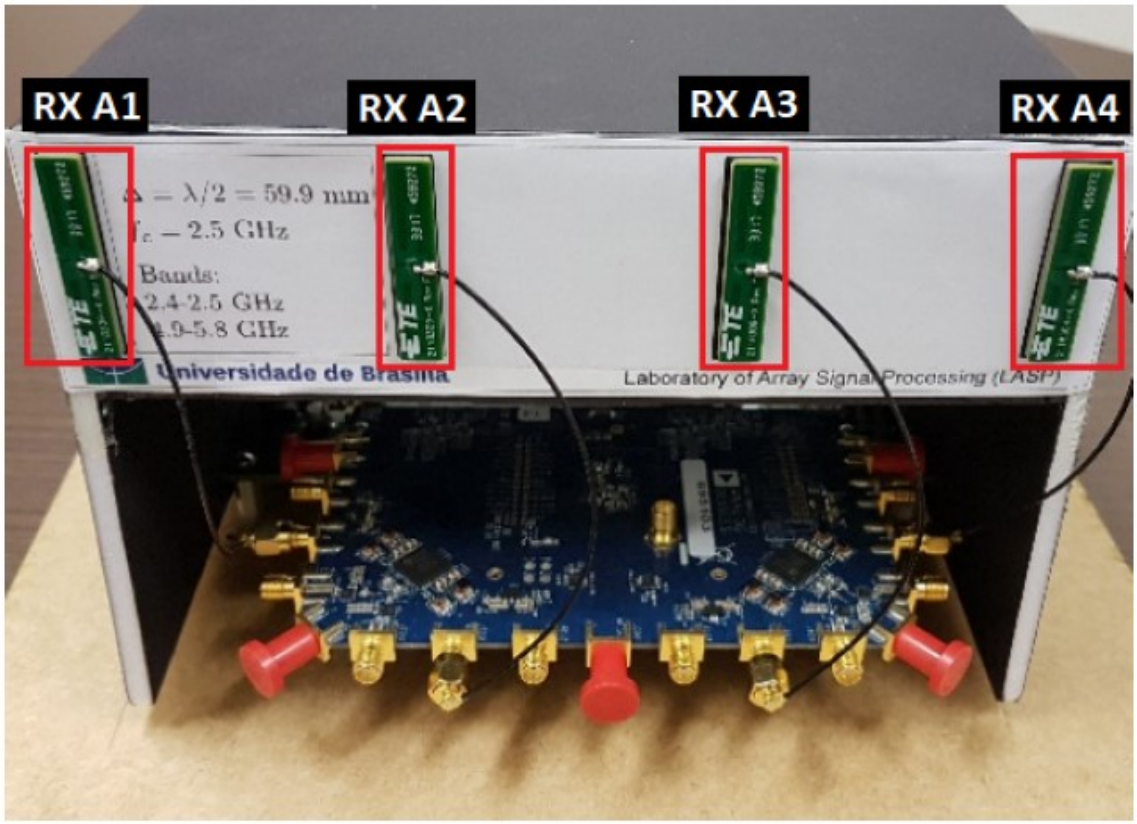

Figure 4.4: Proposed low-cost antenna array-based drone tracking device with 4 element ULA and a 4 x 4 MIMO SDR

4.3 Signal Processing Framework structure

This section is divided in three subsections. Subsection 4.3.1 explains the mathematical approach of the hardware calibration of Section 4.1. Then, Subsection 4.3.2 draws the importance of the filtering. In Subsection 4.3.3 a sample selection approach for DoA estimation by automatic phase deviation detection is proposed, whereas in Subsection 4.3.4 it is presented the DoA estimation framework exploiting pre-processing techniques, model order selection schemes and DoA estimation approaches. Fig. 4.5 depicts the flowchart of proposed signal processing framework solution for DoA estimation.

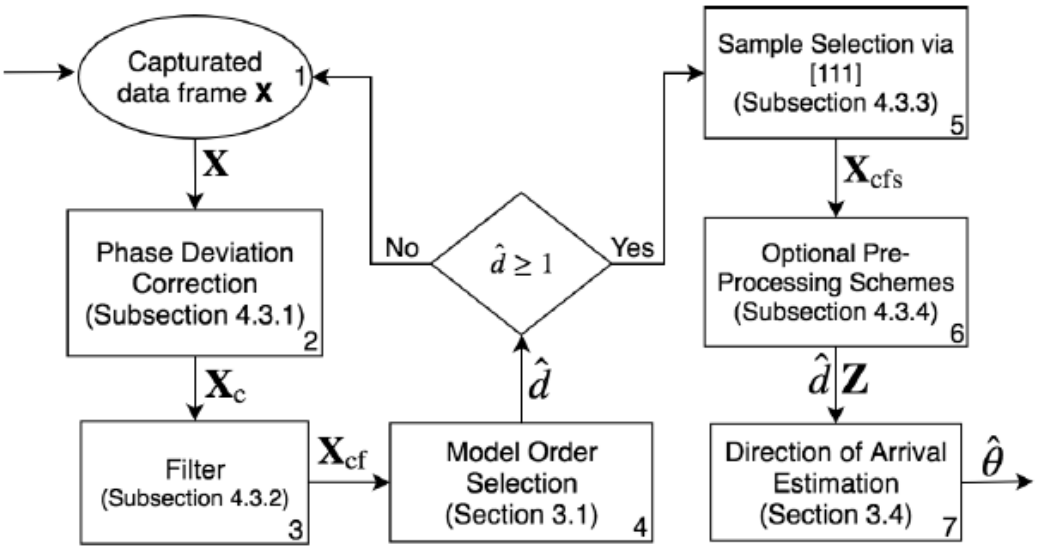

Figure 4.5: Flowchart of proposed framework solution for DoA estimation

As shown in Box 2 of Fig. 4.5, the phase deviation correction proposed on Subsection 4.3.1 returns a matrix Xc that is used in the filter box from Subsection 4.3.2, in order to get an improved data. The returned Xcf is now used in sample selection scheme of Subsection 4.3.3, such as it returns Xcfs that is used for pre-processing schemes and DoA estimation in Subsection 4.3.4.

4.3.1 Phase Deviation Correction

As explained in Section 4.1, several problems may cause phase imbalance. Here it is presented the mathematical approach in order to find the compensation vector such that it corrects the phase shift.

First, the phase of the elements of the matrix $\mathbf{X}$ is extracted by defining

$$\phi_{i,j} = \angle x(i,j) = \arctan\left(\frac{\mathrm{Im}\{x(i,j)\}}{\mathrm{Re}\{x(i,j)\}}\right), \tag{4.1}$$

where $x(i,j)$ is the element in position i,j of the measured matrix $\mathbf{X}$. The operators $\angle$, $\mathrm{Im}\{\cdot\}$ and $\mathrm{Re}\{\cdot\}$ stand for the phase operator, the imaginary part of a complex number and the real part of a complex number, respectively.

In order to compute the phase shift between two channels, the following expression is applied

$$\omega(m,:) = \mathbf{\Phi}(m,:) - \mathbf{\Phi}(i,:) \in \mathbb{C}^{1\times N}, \tag{4.2}$$

where $\mathbf{\Phi}$ stands for the matrix with the phases given by (4.1), i indicates the reference channel and m varies from 1 to M. Since the vector $\omega(m,:)$ is the m-th row of matrix $\mathbf{\Omega}$, in case

$m = i$, the i-th row of $\mathbf{\Omega}$ is filled with zeros. Finally, since the phase difference may slightly vary for different samples in the same row of $\mathbf{\Omega}$ due to the thermal noise, the arithmetic mean of the elements of each row of $\mathbf{\Omega}$ is computed, obtaining the vector $\bar{\omega} \in \mathbb{C}^{M\times 1}$ and its m-th element is given by

$$\bar{\omega}(m) = \frac{1}{N}\sum_{n=1}^{N} \mathbf{\Omega}(m,n). \tag{4.3}$$

Hence, in order to compensate the phase shift between two different channels, the vector $\mathbf{c} \in \mathbb{C}^{M\times 1}$ is computed, whose m-th element is given by

$$\mathrm{c}(m) = \mathrm{e}^{-j\bar{\omega}(m)}. \tag{4.4}$$

Note that the compensation vector $\mathbf{c}$ is computed only once for the system initialization. The calibrated outputs of the antenna array are given by the following expression

$$\mathbf{X}_{\mathrm{c}} = \mathrm{diag}\{\mathbf{c}\}\mathbf{X}, \tag{4.5}$$

where the operator $\mathrm{diag}\{\cdot\}$ transforms its argument vector into the main diagonal of a diagonal matrix.

4.3.2 Band-Rejection Filter

In Chapter 2, the noise is assumed to be Complex Valued Circularly Symmetric Gaussian and identically and independently distributed (i.i.d.). The EFT relies on these properties of the noise. Due to extremely low values of the Pfa presented in Appendix A, the noise behavior is analyzed.

According to Fig. 4.6, the Power Spectrum Density (PSD) is not flat, implying that the noise is time correlated. Note that the hardware inserts a specific noise at 1 MHz. Therefore, and according to third box of Flowchart 4.5 to remove this specific noise a band-rejection filter should be applied at that frequency.

4.3.3 Selection of samples and Matrix X

In order to avoid the unnecessary computational load, when there is no signal present the framework starts a new capture without execute the pre-processing and DoA algorithms. This selection is made by checking the Model Order given by the MOS schemes as presented in Fig. 4.5. Before starting the processing by the pre-processing and DoA algorithms, the authenticity of the data must also be checked. Therefore, if exists a signal present, the captured matrix X is passed to the sampling selection that is explained in this subsection.

As exemplified φ in Fig. 4.7, it is empirically observed that the hardware causes phase

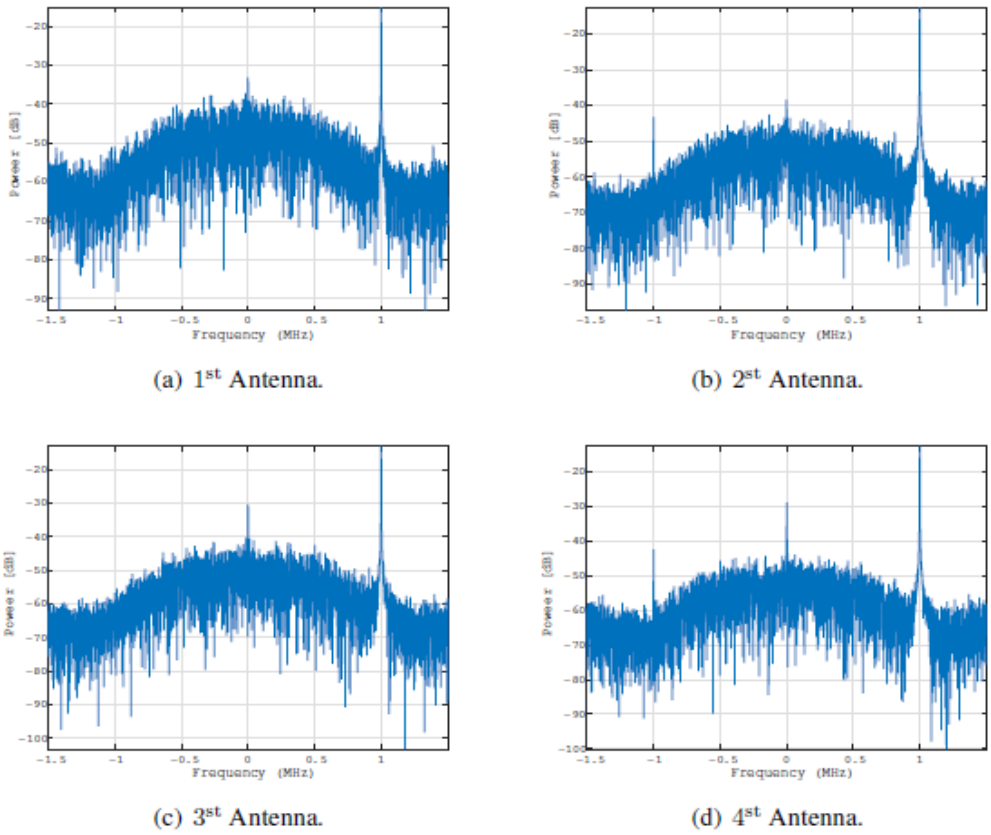

(a) 1st Antenna. (b) 2st Antenna.

(c) 3st Antenna. (d) 4st Antenna.

Figure 4.6: Power Density Spectrum of the noise only case for each antenna.

deviations on the samples in random time instants. Therefore, an approach to select the samples with phase deviations for the DoA estimation is proposed. Note that the phase compensation proposed in Subsection 4.3.1 has been applied on the samples, whose phases are depicted in Fig. 4.7. Furthermore, note that there are significant deviations that can degrade the DoA estimation process. As shown in Fig. 4.8, such ripples can be better visualized by computing the phase difference in the time dimension according to the following expression

$$\gamma(m,i) = (\phi(m,i+1) - \phi(m,i))^2, \tag{4.6}$$

where $\gamma(m,i)$ is the value containing the quadratic difference of two consecutive time samples i and $i+1$ of the m-th channel, and ϕ(m,i) is the element in position m,i of the matrix Φ from (4.1).

By detecting the peaks in Fig. 4.8, it is possible identify which samples should be removed. For this task is used the approach proposed in [19], which returns the value of the threshold. Therefore, the samples whose phase difference are greater than the threshold are

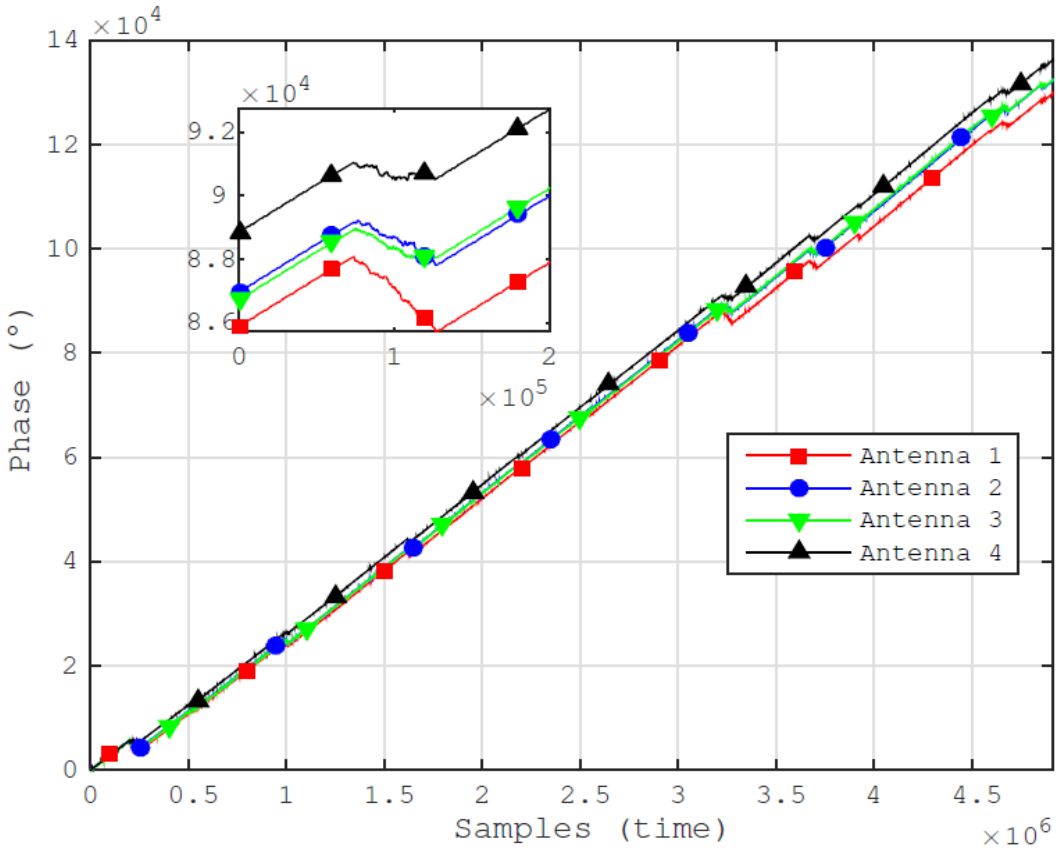

Figure 4.7: Phase of the received data in each antenna. An example of phase deviation region is highlighted in the zoom area.
removed. The result after the samples removed is presented in the following equation

$$\mathbf{X}_{\text{cfs}} = [\mathbf{X}_{\text{cf}}(:, 1 : N_1)|\mathbf{X}_{\text{cf}}(:, N_2 : N_3)|...|\mathbf{X}_{\text{cf}}(:, N_{T-1} : N_T)], \tag{4.7}$$

where $\mathbf{X}_{\text{cfs}}$ is the matrix with the selected samples. Note that $N_T = N$ and the values of $\mathbf{N}_t$, for $t = 1, ..., T$, are found by comparing the phase difference values with the threshold in Fig. 4.8.

4.3.4 MOS, Pre-processing and DoA Estimation

According to box 1 Fig. 4.5, the matrix $\mathbf{X}_{\text{cfs}}$ given in Subsection 4.3.3 is used now to improve the DoA estimation with pre-processing schemes. There are several DoA estimation schemes in the literature as presented in Section 3.3, such as beamforming approaches and subspace based approaches. In this framework, all the DoA methods presented in the Section 3.3 are adopted, since the redundancy brings confidence and after the pre-processing schemes the DoA methods have similar performance, as presented in Section 5.4.

The DoA estimation schemes assume that the model order d is known. In practice, model order selection techniques should be applied to estimate the model order d as depicted in Fig.

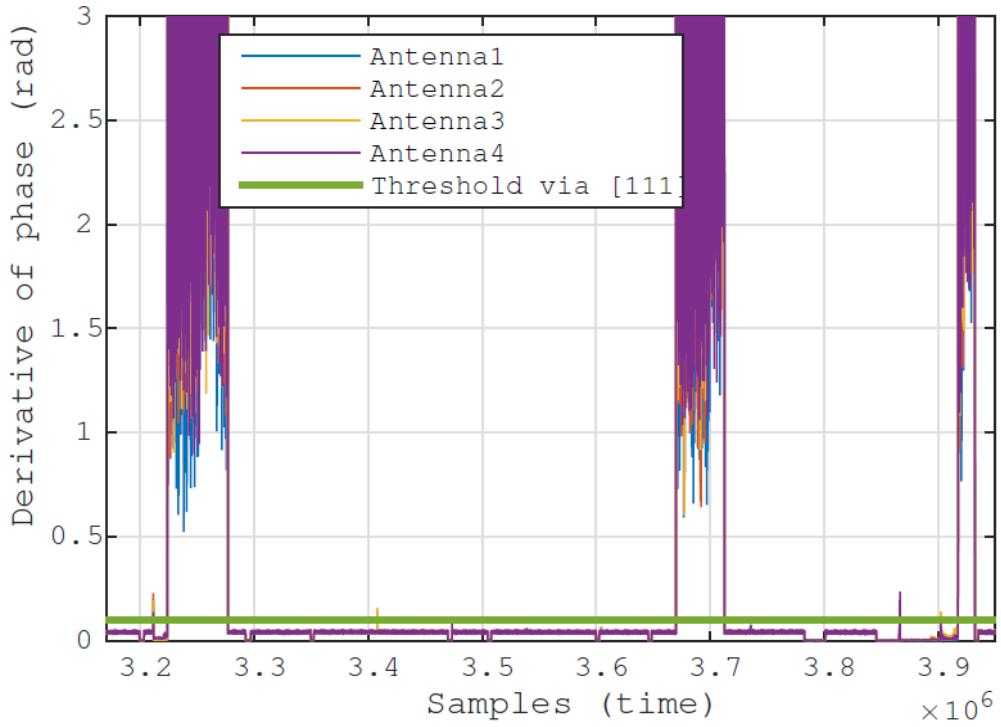

Figure 4.8: Phase difference between consecutive samples from Fig. 4.7.

4.5.

In the box 4 from Fig. 4.5, the Exponential Fitting Test (EFT) [20, 6] was adopted as the model order selection scheme. The EFT has the deflation properties that allows to find suitable thresholds as a function of the Probability of False Alarm (P_{fa}). By exploiting the deflation property and by finding suitable thresholds, the EFT has been the only scheme in the literature to estimate d = 1 in the presence of a strong LOS signal and d = 0, in the noise-only measurements. Several schemes were compared in the literature such as Akaike Information Criterion (AIC) [1], Efficient Detection Criterion (EDC) [3], Minimum Description Length (MDL) [2], Stein's unbiased risk estimate (SURE) [4], RADOI [5], Estimation Error (ESTER) [7] and Subspace-based Automatic Model Order Selection (SAMOS) [8]. The M-EFT [20, 6, 21] has been also suitable, but a smaller P_{fa} was required to find the thresholds. The calculus of the thresholds of the EFT requires an extremely low P_{fa}. Such calculus is computationally prohibitive. Therefore, in Appendix A it is proposed an extrapolation algorithm to compute such thresholds. Note that our proposed extrapolation algorithm has been applied in [22, 23, 24], although no details are provided in these works. Note that the reason for extremely low P_{fa} may be related to the colored noise behavior presented in

Subsection 4.3.2.

In order to further improve the accuracy of DoA estimation, pre-processing schemes can be applied beforehand. In this work the Spatial Smoothing (SPS) [9, 25], Forward Backward Averaging (FBA) [10, 11] and Vander mode In variation Technique (VIT) [12] were used as pre-processing schemes. The box 6 from Fig. 4.5 is now enlarged in Fig. 4.9 in order to best describe the pre-processing step. After that, a matrix Z is returned and used by the DoA methods summarized in Section 3.3.

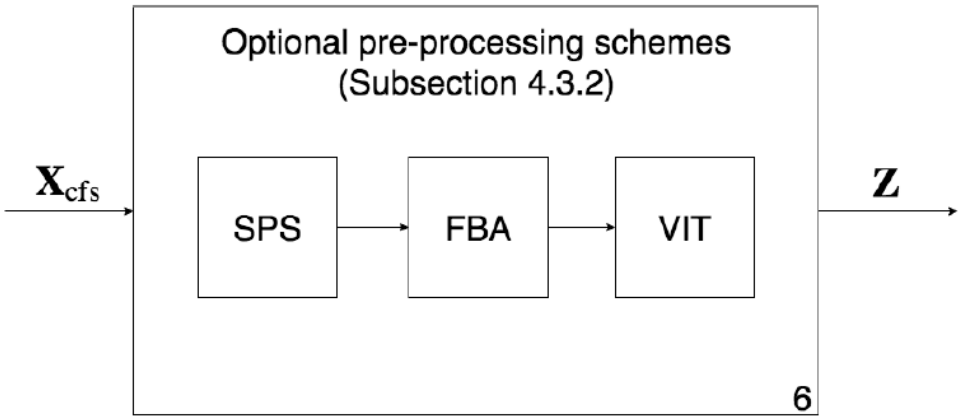

Figure 4.9: Expanded version of box 6 presented in Fig. 4.5

5.Results

In this Chapter, the proposed drone tracking device with measurement campaigns in an outdoor scenario, is validated. In Section 5.1, the setup for the measurement campaign is described, while, in Section 5.2, 5.3, and 5.4, are presented the results for the filter, MOS and DoA respectively.

5.1 Experimental Setup

In Figure 5.1(a), it is depicted the outdoor scenario used for the measurement campaigns. On the right side, was placed the drone tracking device proposed in Section 4 as the receiver, while, on the left side, the transmitter is placed. The transmitter, that simulates an UAV, is a 2x2 MIMO SDR platform ASPR4 [26], with 50 MHz to 6.0 GHz, a channel bandwidth of 200 kHz to 56 MHz and max power of 10 dBm at each output port. The center frequency of both transmitter and antenna array-based receiver was set at 2.48 GHz.
As shown in Figure 5.2, the distance between the transmitter and the receiver is 48 m. Both transmitter and receiver are on tripods 115 cm above the ground. Note that the red "X" in Figure 5.2 is the location from where the photo in Figure 5.1(a) has been taken.
The transmitter was setup using a MSK message signal to verify that the device functions properly. The transmitted symbols are pseudo random sequences with 1024 bits, a header 0xFFFF and a footer 0x0000. The proposed drone tracking device was setup to a 1 MHz of bandwidth, 3 MHz sampling frequency, 2:48 GHz carrier frequency, 500 kpbs data rate and 5120 samples.
As shown in Figure 5.2, the transmitter is fixed, and the receiver rotates from +90_ to -90_ in steps of 10_. Note that this step is done manually, so the estimated DoA may be biased due to inaccuracies of the operator controlling the rotation, or even printing error in the paper-based protractor presented in Figure 5.1(b).

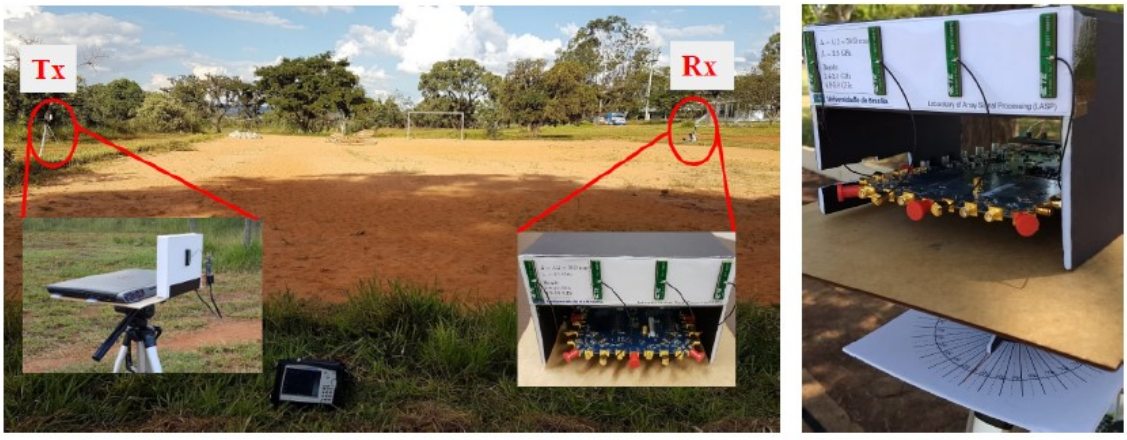

(a) Positions of the transmitter and antenna array based receiver

(b) Assembled array with paper-based protractor

Figure 5.1: Photos taken during the measurement campaigns of the outdoor scenario.

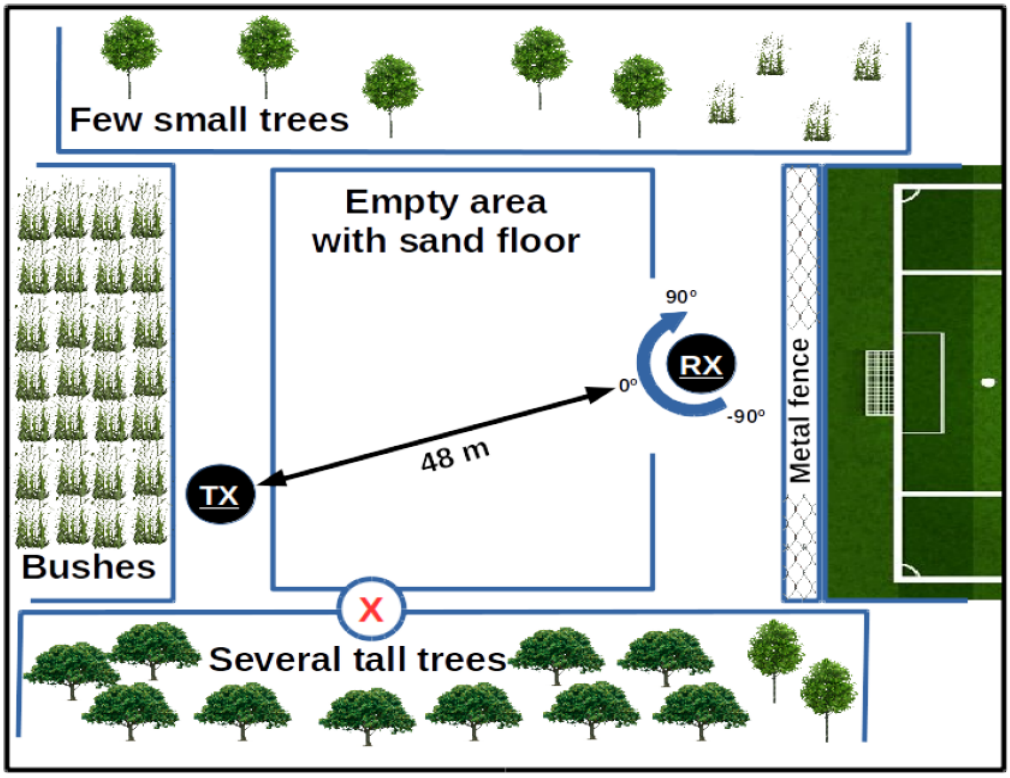

Figure 5.2: Top view of the outdoor scenario for the measurement campaigns including the positions of the transmitter and of the antenna array based receiver

5.2 Band-Reject Filter Results

As presented in the Subsection 4.3.2, it is important to filter the received signal in order to obtain a Gaussian behavior. In Figs. 5.3 and 5.4, it is depicted the histogram for antenna 1, 2, 3 and 4, with and without the filtering. The improvement with the filter is noted with the Gaussian behavior presented in Fig. 5.4 with the data after filtering.

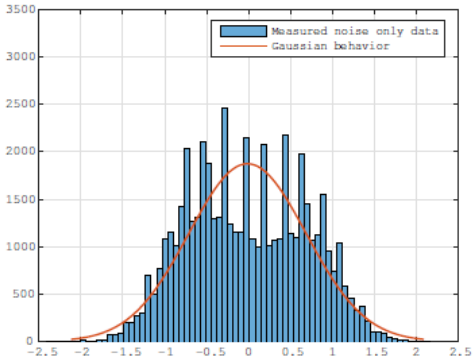

(a) 1^{st} Antenna with 70 bins, mean $= -0.1035$ and Standard deviation $= 0.7018$.

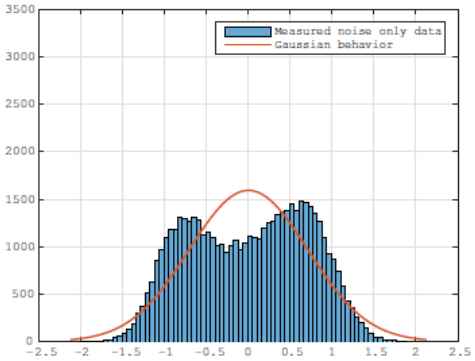

(b) 2^{st} Antenna with 70 bins, mean $= -0.0494$ and Standard deviation $= 0.6322$.

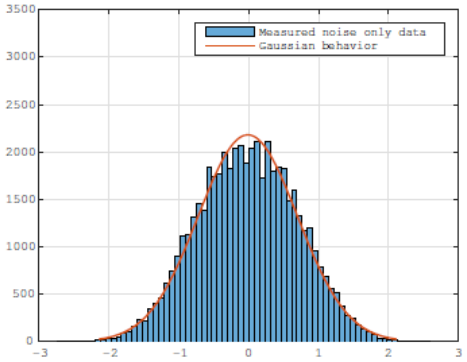

(c) 3^{st} Antenna with 70 bins, mean $= 0.1162$ and Standard deviation $= 0.7377$.

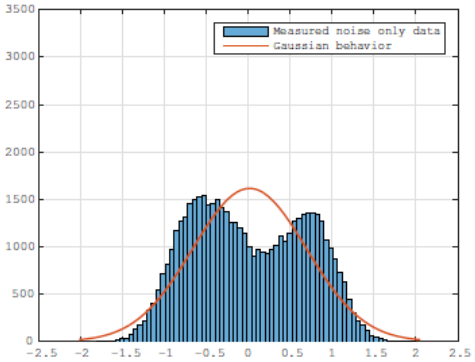

(d) 4^{st} Antenna with 70 bins, mean $= 0.0845$ and Standard deviation $= 0.6836$.

Figure 5.3: Histogram of the noise only case for each antenna.

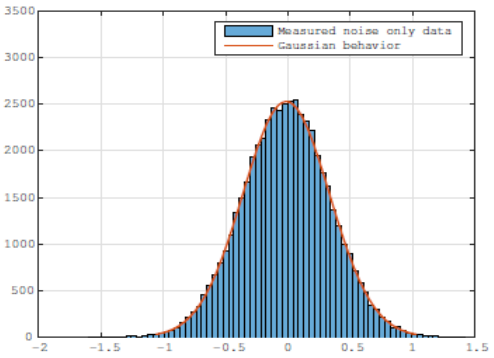

(a) 1^{st} Antenna with 70 bins, mean $= -0.1035$ and Standard deviation $= 0.7018$.

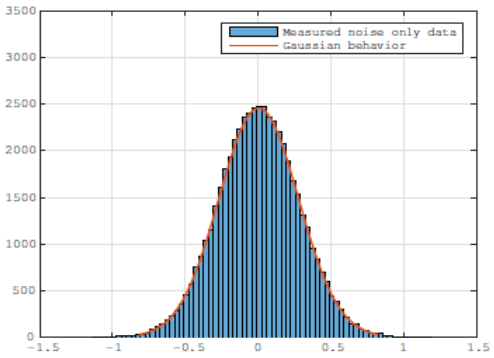

(b) 2^{st} Antenna with 70 bins, mean $= -0.0494$ and Standard deviation $= 0.6322$.

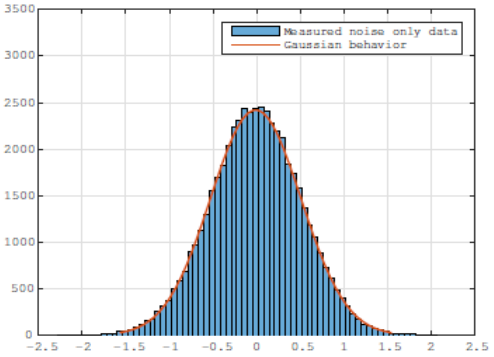

(c) 3^{st} Antenna with 70 bins, mean $= 0.1162$ and Standard deviation $= 0.7377$.

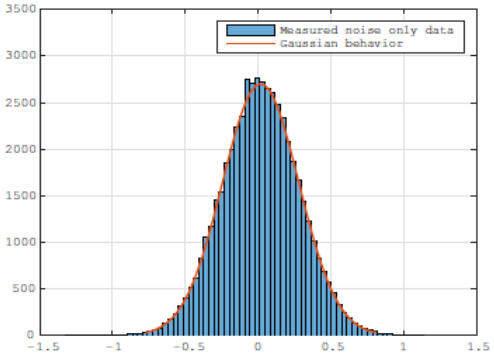

(d) 4^{st} Antenna with 70 bins, mean $= 0.0845$ and Standard deviation $= 0.6836$.

Figure 5.4: Histogram of the filtered noise only case for each antenna.

3 MOS Results

The Model Order Selection (MOS) schemes are very important on High Resolution Signal Processing as well in our proposed device. As explained in Subsection 4.3.3 and 4.3.4 the MOS is used for DoA schemes and to select a data frame that would be processed in order to avoid unnecessary data processing if the signal source is not present. The third block of Flowchart from Fig. 4.5 give the matrix X_{cf} which is used by MOS schemes.
Two experiments to test the MOS schemes were done. The first experiment used a transmitter 2x2 MIMO SDR platform ASPR4 [26] with max power of 10 dBm, which transmit a known signal continuously. In the other hand, the second experiment try to be more realistic and, as presented in Table 1.1, a signal transmitted by an UAV uses WiFi to communicate with the controller and can be simulated by any router, was used [27]. Other advantage of the second experiment is the noise case only, with no sources. These experiments used only one transmitter, so the model order must be always one when a signal is present.
In order to become easier to see, the results is divided into two images for each experiment campaign is presented in Fig. 5.5 and the second experiment is presented in Fig. 5.6, with the behavior of the methods presented in Section 3.1. Note that the first two figures contain the power and eigenvalues, in addition to the figures with the MOS results. With these two images it is possible to see the behavior over time and compare when a signal is received and when there is only noise.

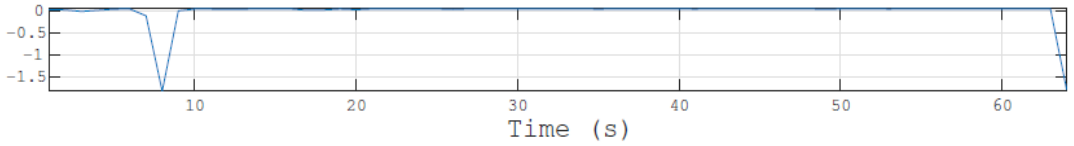

(a) Average normalized power (dB) of the 4 antennas from captured data on outdoor campaign

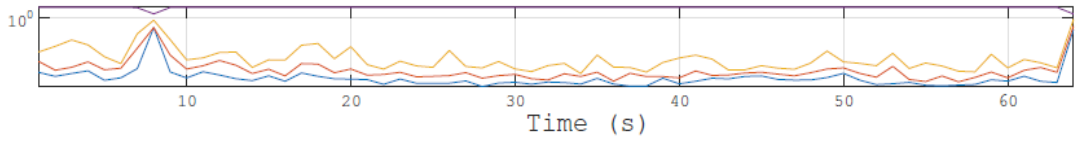

(b) Four Eigen Values (dB) from captured data on outdoor campaingn

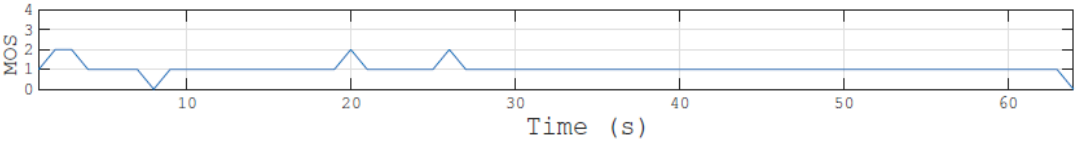

(c) EFT [6] using thresholds from Appendix A

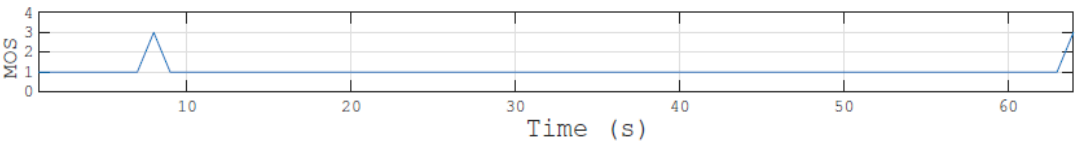

(d) Radoi-EDC

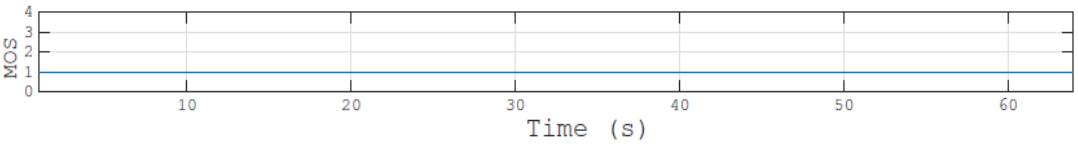

(e) SAMOS [8]

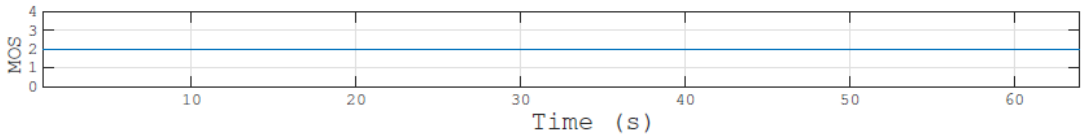

(f) Radoi [5]

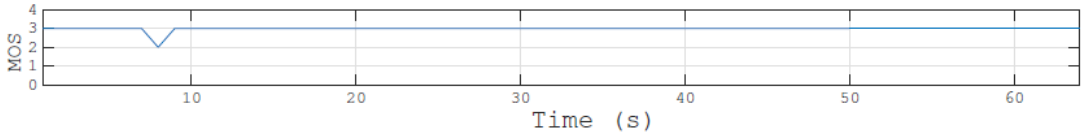

(g) EDC [3]

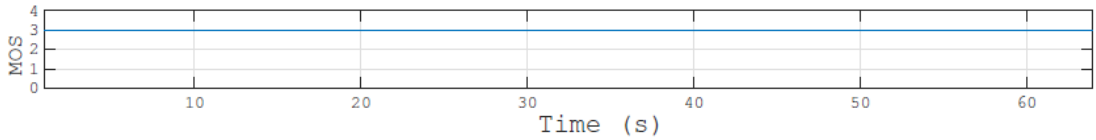

(h) Akaike [1]

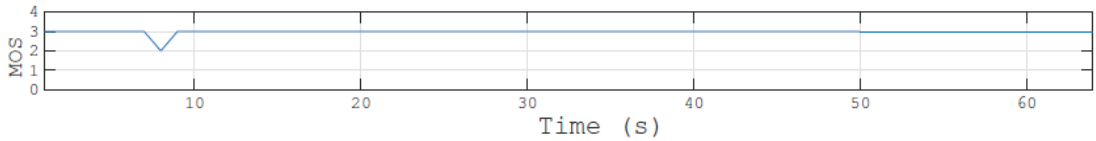

(i) MDL [2]

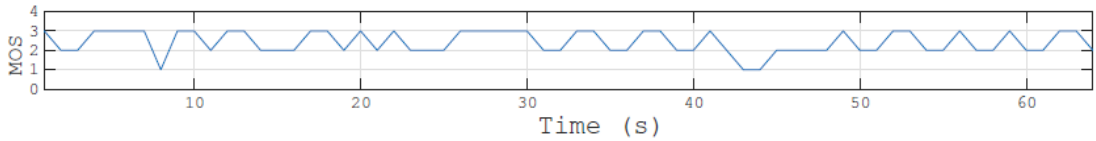

(j) Modified EFT [21]

Figure 5.5: First experiment to calculate the MOS by schemes from 3.1 using an ASRP4 [26] as transmitter.

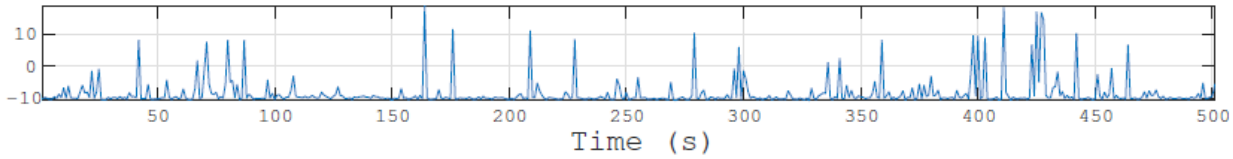

(a) Average normalized power (dB) of the 4 antennas from captured data on outdoor campaingn

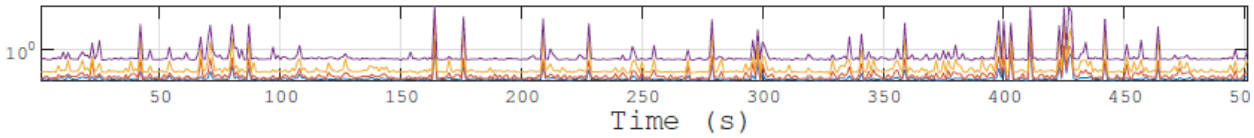

(b) Four eigen values from captured data on outdoor campaingn

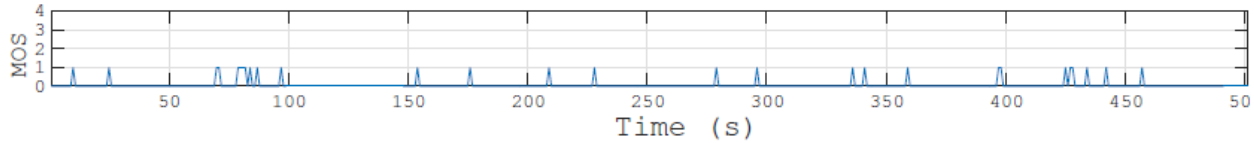

(c) EFT [6] using thresholds from Appendix A

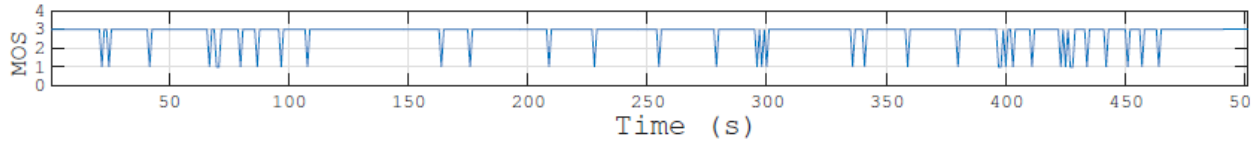

(d) Radoi-EDC

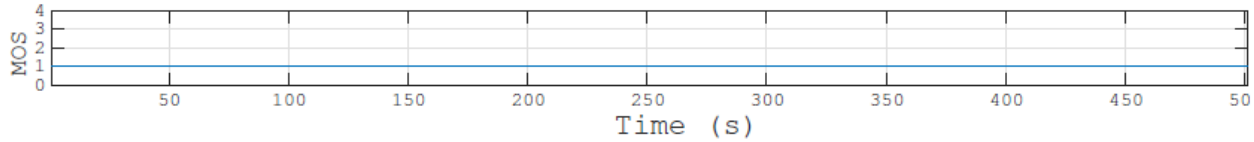

(e) SAMOS [8]

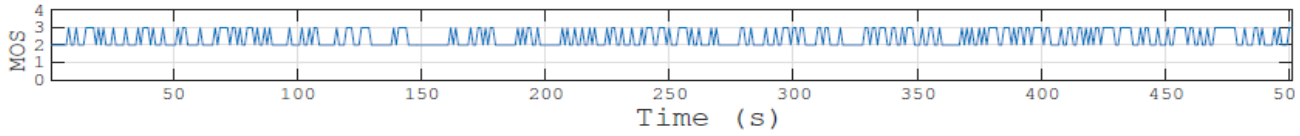

(f) EDC [3]

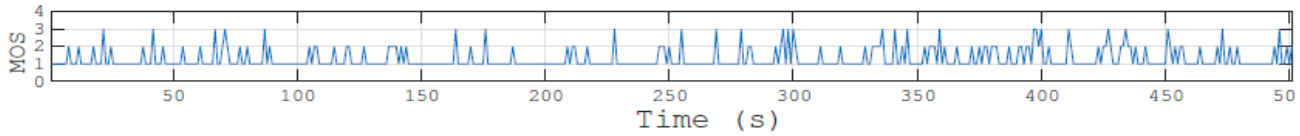

(g) Modified EFT [21]

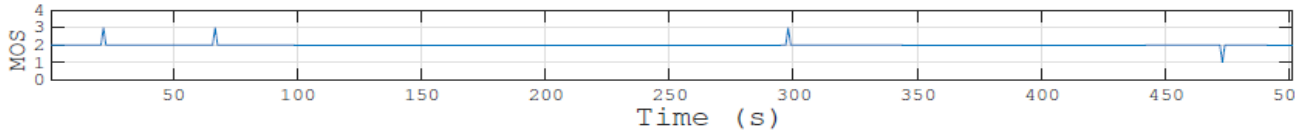

(h) Radoi [5]

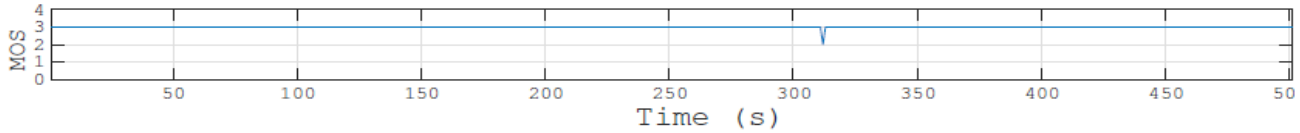

(i) Akaike [1]

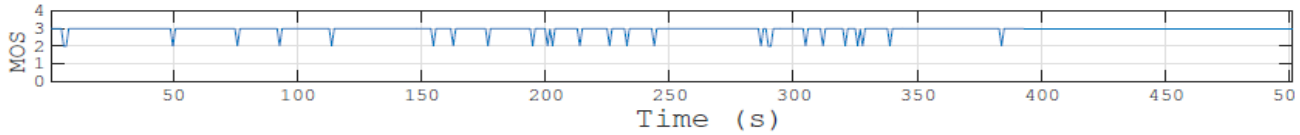

(j) MDL [2]

Figure 5.6: Second experiment to calculate the MOS by schemes from 3.1 using a router [27] as transmitter.

Except for SAMOS [8] and ESTER [7], the X_{cf} has 5120 samples. The computational processing of Singular Value Decomposition (SVD) is very prohibitive for large matrices, therefore, was used a matrix X_{cf} 2 C_{4_1000} matrix for SAMOS and ESTER.

Despite some minor errors, the EFT using the proposed thresholds from Appendix A has the best performance based on the fact that the recognized number of sources was one. The Radio with discriminant approach also stands out at the point where in presence of a signal it recognized the best amount of frames. However, as presented in the Fig. 5.6(d) of the second experiment, in the noisy case only it detects the wrong number of sources.

5.4 DoA Results

This Section shows the performance of the DoA schemes shown in Section 3.3 using the ASRP4 [26] as transmitter. During the measurement campaign, the achieved Bit Error Rate (BER) was 10^{-4}.

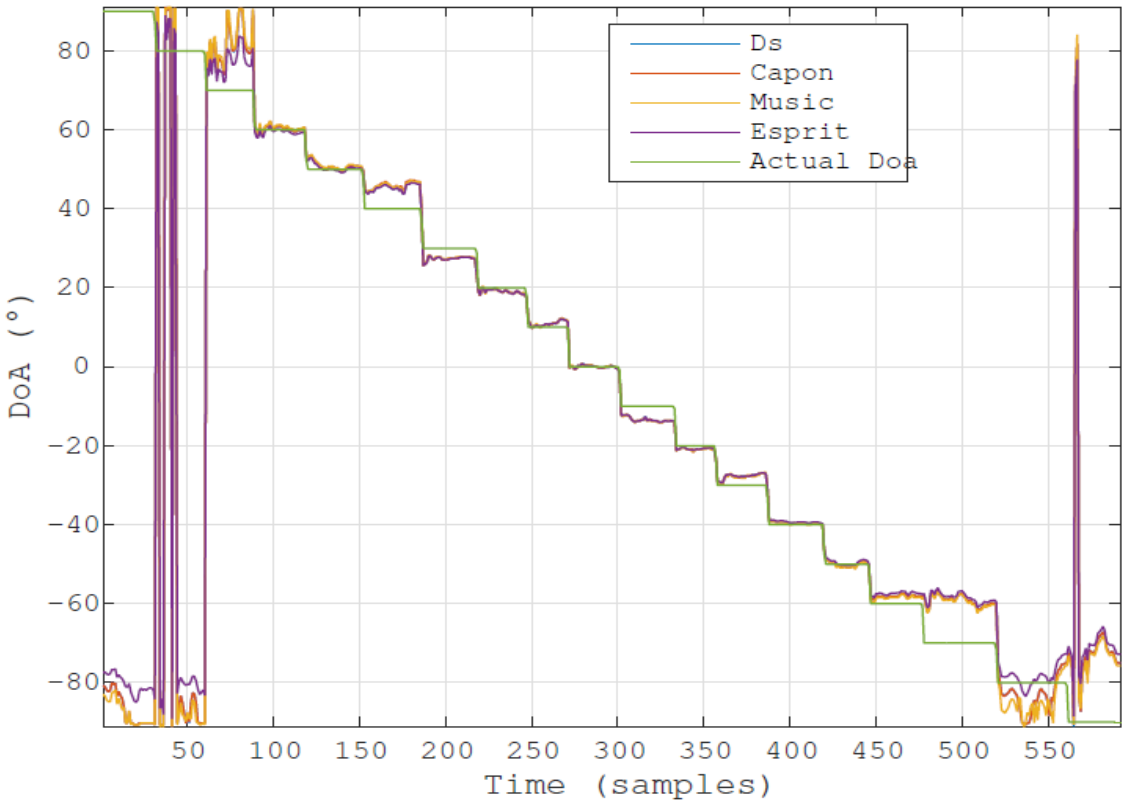

Figure 5.7: Comparison between the DoA estimation schemes by varying the DoA from +90° to -90° with steps of 10°.

Fig. 5.7 shows the DoA calculated by rotating the base array over the time. Note that our proposed device works properly for a DoA ranging from -60° to 60°. The RMSE, given by Eq. 5.1, of DoA methods combined with pre-processing schemes is shown in Fig. 5.8. The worst algorithm DoA error was about 6° on this range of -60° to +60°. The equation for RMSE is given by

$$\mathrm{RMSE}(\theta_1) = \sqrt{\frac{1}{Q}\sum_{q=1}^{Q}(\theta_1^{(q)} - \hat{\theta}_1^{(q)})^2} \tag{5.1}$$

where q stands for one of a total of Q realizations for each 10° step of the measurement campaign. In each 10° step, many frames of N = 5120 snapshots are acquired for each channel, giving us the matrix $\mathbf{X} \in \mathbb{C}^{4\times 5120}$.

The evolution of the results from the range of -60° to +60° is presented into Tables 5.1, 5.2, 5.3, 5.4, 5.5 and 5.6, which present the results increasing with the use of the pre-processing schemes.

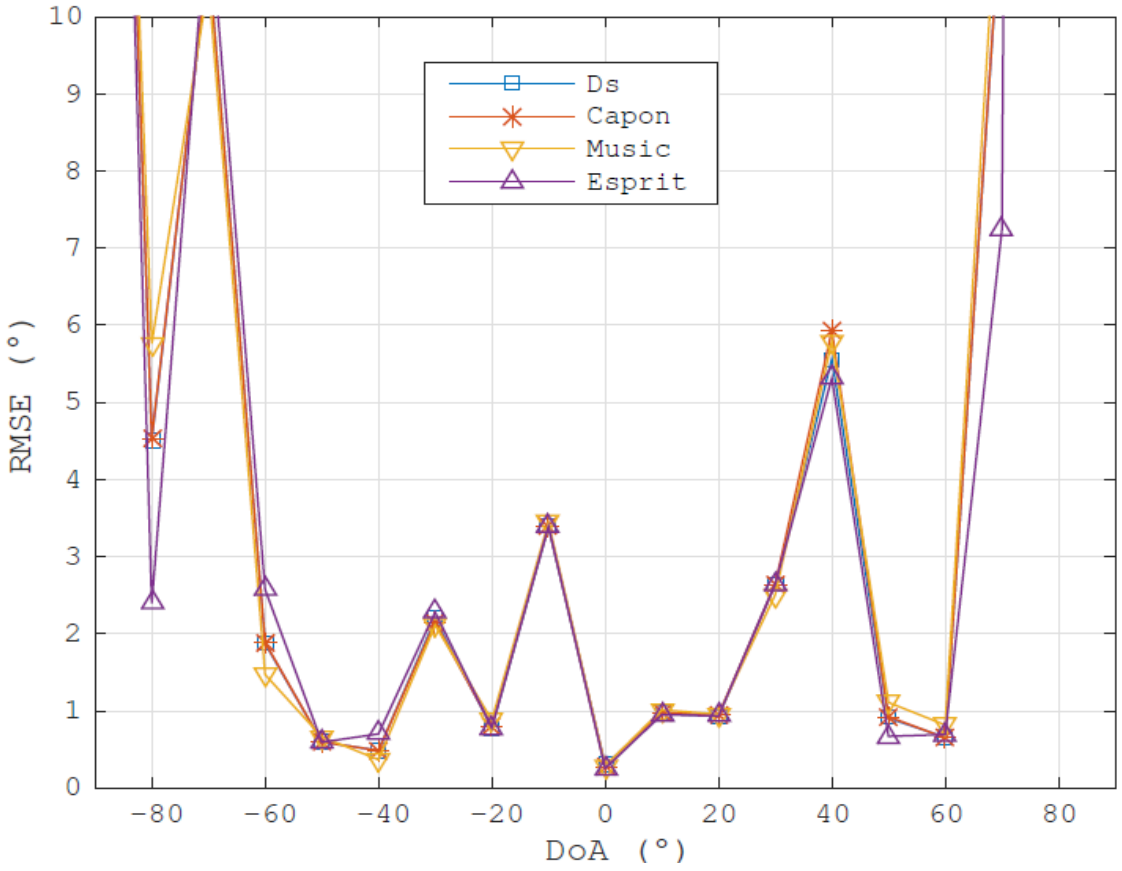

Figure 5.8: RMSE comparison between the Expected DoA and the DoA estimation combined with pre-processing schemes by varying the angle from +90° to -90° with steps of 10°.

Table 5.1: RMSE for the schemes in Section 3.2 without the pre-processing schemes, using the measurements from Fig. 5.7

Algorithm	DS	CAPON	MUSIC	ESPRIT
RMSE	2.3388°	1.6696°	3.9923°	2.8080°
Variance of the RMSE	4.2826°	1.0706°	11.5493°	4.0692°

Table 5.2: RMSE for the schemes in Section 3.2 with VIT [12] pre-processing scheme, using the measurements from Fig. 5.7

Algorithm	DS	CAPON	MUSIC	ESPRIT
RMSE	2.3388°	2.0242°	2.8352°	2.9575°
Variance of the RMSE	4.2861°	1.8770°	4.8320°	5.2364°

Table 5.3: RMSE for the schemes in Section 3.2 with FBA [10, 11] pre-processing scheme, using the measurements from Fig. 5.7

Algorithm	DS	CAPON	MUSIC	ESPRIT
RMSE	2.1205°	1.6833°	4.0570°	2.4022°
Variance of the RMSE	3.7932°	1.0795°	16.7736°	3.6046°

Table 5.4: RMSE for the schemes in Section 3.2 with SPS [9, 25] pre-processing scheme, using the measurements from Fig. 5.7

Algorithm	DS	CAPON	MUSIC	ESPRIT
RMSE	1.6484°	2.4197°	1.9689°	1.8716°
Variance of the RMSE	2.3307°	2.4003°	3.6663°	1.8416°

Table 5.5: RMSE for the schemes in Section 3.2 with FBA and SPS pre-processing schemes, using the measurements from Fig. 5.7

Algorithm	DS	CAPON	MUSIC	ESPRIT
RMSE	1.6548°	1.6745°	1.6813°	1.8776°
Variance of the RMSE	2.3628°	2.5452°	2.4180°	1.8904°

Table 5.6: RMSE for the schemes in Section 3.2 with FBA, SPS and VIT pre-processing schemes, using the measurements from Fig. 5.7

Algorithm	DS	CAPON	MUSIC	ESPRIT
RMSE	1.6361°	1.6676°	1.6475°	1.6757°
Variance of the RMSE	2.2671°	2.5168°	2.3600°	2.1913°

Finally, the performance evolution result RMSE presented in tables 5.1, 5.2, 5.3, 5.4, 5.5 and 5.6 is now drawn in Fig. 5.9. These results show the importance of preprocessing schemes, which proves that it is better to use all of them in combination.

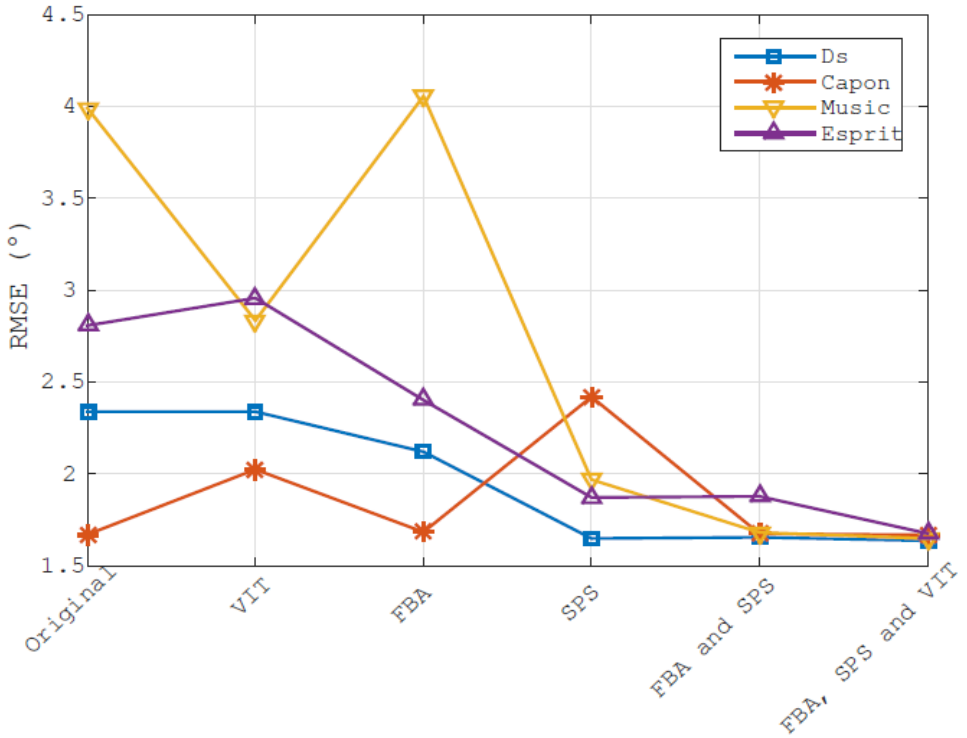

Figure 5.9: Comparison of performance between the RMSE results presented in tables 5.1, 5.2, 5.3, 5.4, 5.5, 5.6

As shown in Table 5.7, the total cost of the proposed drone tracking solution is US$ 2.222, while the solutions in [28] and [29] cost US$ 226.000 and US$ 120.000, respectively. Therefore, our proposed off-the-shelf solution costs less than 2 % of the commercial solutions in [28] and [29].

Table 5.7: Price Table for the Hardware of the Proposed Drone Tracker Device

Hardware	Cost (US$)
AD-FMCOMMS5-EBZ-ND [30]	1080
4 × Dual-Band Antenna 2.4 & 5GHz [18]	11
ZYNQ 7000 Zc702 [31]	999
Power Divider 2.4-6GHz 30Watts RoHS IP67 [32]	109
5 × cable 305mm HPP100 SMA [33]	23
Total	2222

6. Conclusion

Over the last years, Unmanned Aerial Vehicles (UAVs) have been a major concern of airspace control bodies and military due to terrorist attacks and illegal activities. Therefore, recently police forces and security companies have drawn their attention to drone tracking devices in order to provide the safeness of citizens and clients. Consequently, applications of direction of arrival (DoA) techniques have dramatically increased in various areas. In this sense, the development of low-cost devices for drone tracking is fundamental to fit such demands.

In this thesis, was proposed a low-cost antenna array-based drone tracking device for outdoor environments. The proposed solution is divided into hardware and software parts. The hardware of the proposed device is based on off-the-shelf components such as an omnidirectional antenna array, a power division component, four SMA cables, a 4 channel SDR platform with 70 MHz to 6.0 GHz, a FPGA motherboard and a laptop. The software part includes state-of-the-art algorithms for model order selection (MOS), pre-processing and DoA estimation. The performance of the proposed low-cost solution was evaluated in outdoor scenarios. According to our measurement campaigns, it is shown that, when the transmitter is in the front fire position, i.e., with a DoA ranging from -60_ to 60_, the maximum and the average DoA errors are 6_ and 1,6_, respectively. Our proposed off-the-shelf solution costs less than 2 % of commercial solutions in [28] and [29]. This work also makes a comparative approach between several state-of-the-art MOS algorithms in order to choose the method with best performance, which is used in the proposed device. Despite some minor errors, the state-of-the-art EFT [6] algorithm, using the proposed thresholds from Appendix A, had the best performance and was used for MOS. Additionally, presents individual results of improvement brought by each pre-processing algorithm and its influence on the accuracy of the DoA estimation. It was proved that the DoA methods have a better accuracy with all the pre-processing schemes such as FBA [10, 11], SPS [9] and VIT [12], used in combination with each other.

One of the big problems on practical antenna arrays is phase imbalance between the in-

puts of the SDR. The presented calibration process aims to solve this problem. Due to minor random errors caused by the hardware, was also included others specific pre-processing steps in order to remove the data disturbed, the colored noise and consequently increase the DoA accuracy.

The DoA estimation used the Delay and Sum [13], CAPON [14], MUSIC [15] and ESPRIT [16] algorithms, and their accuracy was measured. The DoA methods basically had similar performance, however, ESPRIT spends more computational load. Without preprocessing, MUSIC was the one with the highest variance and the worst measured error.

It was also proved that it is highly possible to detect the direction of an UAV with an array of antennas built with low-cost hardware and without concern about complex issues such as mutual coupling or calibration in environments with optimal conditions. It is clear that some improvements can be made, such as to use a more realistic noise model given the low Pf_a, and to use some electronic instrument to allow bias reduction, as shown in Section

5.1. However, for our motivation, UAVs can be detected with good accuracy in the range of -60 to +60 degrees.

THANK YOU

Plot no 10 Shiv Vihar A Block Najafgarh Nala Road Vikasnagar Uttam Nagar New Delhi-110059